Monthly Notices of the ROYAL ASTRONOMICAL SOCIETY
MNRAS **499,** 3868–3883 (2020) doi:10.1093/mnras/staa2798

A search for optical and near-infrared counterparts of the compact binary merger GW190814

A. L. Thakur [1,2★] S. Dichiara [3,4] E. Troja [3,4] E. A. Chase,[5,6,7,8] R. Sánchez-Ramírez [1] L. Piro [1] C. L. Fryer,[5,9,10,11,12,13] N. R. Butler,[14] A. M. Watson [15] R. T. Wollaeger,[5,10] E. Ambrosi,[16] J. Becerra González,[17,18] R. L. Becerra [19] G. Bruni [1] S. B. Cenko,[4,20] G. Cusumano,[16] A. D'Aì,[16] J. Durbak,[3] C. J. Fontes [5,6] P. Gatkine,[3] A. L. Hungerford,[5,6,9] O. Korobkin [5,9,10] A. S. Kutyrev,[4] W. H. Lee,[15] S. Lotti,[1] G. Minervini,[1] G. Novara,[21,22] V. La Parola,[16] M. Pereyra,[23] R. Ricci,[24,25] A. Tiengo [21,22,26] and S. Veilleux[3]

Affiliations are listed at the end of the paper

Accepted 2020 September 10. Received 2020 September 10; in original form 2020 July 6

ABSTRACT

We report on our observing campaign of the compact binary merger GW190814, detected by the Advanced LIGO and Advanced Virgo detectors on 2019 August 14. This signal has the best localization of any observed gravitational wave (GW) source, with a 90 per cent probability area of 18.5 deg^2, and an estimated distance of ≈240 Mpc. We obtained wide-field observations with the Deca-Degree Optical Transient Imager (DDOTI) covering 88 per cent of the probability area down to a limiting magnitude of $w = 19.9$ AB. Nearby galaxies within the high probability region were targeted with the Lowell Discovery Telescope (LDT), whereas promising candidate counterparts were characterized through multicolour photometry with the Reionization and Transients InfraRed (RATIR) and spectroscopy with the Gran Telescopio de Canarias (GTC). We use our optical and near-infrared limits in conjunction with the upper limits obtained by the community to constrain the possible electromagnetic counterparts associated with the merger. A gamma-ray burst seen along its jet's axis is disfavoured by the multiwavelength data set, whereas the presence of a burst seen at larger viewing angles is not well constrained. Although our observations are not sensitive to a kilonova similar to AT2017gfo, we can rule out high-mass (>0.1 $M_\odot$) fast-moving (mean velocity ≥0.3c) wind ejecta for a possible kilonova associated with this merger.

Key words: (*transients*:) black hole - neutron star mergers – stars: neutron – stars: black holes.

1 INTRODUCTION

The era of gravitational wave (GW) astronomy started with the discovery of GW150914 (Abbott et al. 2016), which provided the first direct GW detection from a compact binary coalescence (CBC). The signal was generated by the merger of a binary black hole (BBH) to form a single black hole. Two years later, the detection of a GW signal from a binary neutron star (BNS) merger (GW170817; Abbott et al. 2017a) led to another fundamental breakthrough. The detection of the short gamma-ray burst (sGRB) and kilonova (GRB 170817A and AT2017gfo, respectively; Abbott et al. 2017b) associated with GW170817 provided the first observations of the electromagnetic (EM) counterparts of a GW source. During the first (O1) and second (O2) observing runs of the Advanced LIGO (Aasi et al. 2015) and Advanced Virgo (Acernese et al. 2015) detectors, 11 confirmed detections of GW signals from CBCs were reported, of which, ten were BBH mergers and one was a BNS merger (Abbott et al. 2019). The third observing run (O3) started on 2019 April 1 and was suspended on 2020 March 27. At the time of writing, O3 data have produced four confirmed detections (GW190412, GW190425, GW190521, GW190814; Abbott et al. 2020a,b,c,d, respectively) and 54 unretracted candidate signals.[1]

GW190814 was observed on 2019 August 14 at 21:10:39 UTC. The initial analysis with BAYESTAR (Singer & Price 2016) used data from the LIGO-Livingston and Virgo detectors, which resulted in a 90 per cent localization area of 772 deg^2 and mean distance of 276 Mpc with a standard deviation of 56 Mpc. Data from the LIGO-Hanford detector were later added to the analysis and resulted in an updated 90 per cent localization value of 38 deg^2. The candidate was initially assigned a high probability mass-gap classification based on preliminary analysis (>99 per cent; LVC 2019a). A mass-gap classification suggests that the mass of at least one of the binary components is between 3 and 5 $M_\odot$. Upon further analysis with LALInference (Veitch et al. 2015), the signal classification was updated to a neutron star–black hole (NSBH) merger (LVC 2019b). The mass of the lighter object was reported to be <3 $M_\odot$ and the mass of the heavier object to be >5 $M_\odot$. The NSBH classification was based on the assumption that the heavier object is a black hole

★ E-mail: aishwarya.thakur@inaf.it

[1] https://gracedb.ligo.org/superevents/public/O3/.

and the lighter object is a neutron star. The localization and distance estimate were also refined during this analysis with an updated distance estimate of 267 (±52) Mpc and a 90 per cent (50 per cent) localization value of 23 (5) $\deg^2$. These values were only slightly modified in the final analysis, presented in Abbott et al. (2020d). The median distance reported for this merger is 241^{+41}_{-45} Mpc, and its localization further improved to 18.5 $\deg^2$(90 per cent). The heavier object is a BH with mass $23.2^{+1.1}_{-1.0}\,M_\odot$, whereas the lighter object, with a mass of $2.6^{+0.08}_{-0.09}\,M_\odot$, is not unambiguously classified.

The low false-alarm rate (FAR) and its preliminary association to an NSBH merger make GW190814 an event of considerable interest, although the mass of the lighter object does not rule out a BBH. The localization area for this event is the best for any GW signal so far, and allowed for extensive follow-up observations to search for possible electromagnetic (EM) counterparts (e.g. Dobie et al. 2019; Ackley et al. 2020; Andreoni et al. 2020).

The detection of any EM counterpart helps improve the localization of a GW signal while simultaneously providing information on the physics of the merger and its environment (Abbott et al. 2017a). Whereas the EM signatures of a BBH merger (e.g. Graham et al. 2020; Abbott et al. 2020b) are uncertain, the possible counterparts of an NSBH merger should be in many ways similar to the EM signals associated to BNS mergers. A short duration gamma-ray burst (sGRB), produced by a relativistic jet launched from the merger remnant, may be visible soon after the merger (e.g. GRB 170817A; Abbott et al. 2017b). The interaction of this relativistic jet with the circumburst environment produces afterglow emission, observable across the EM spectrum (e.g. Hallinan et al. 2017; Troja et al. 2017).

Dynamical ejecta and subrelativistic wind outflows produce a distinctive EM signal known as a kilonova (KN; Li & Paczyński 1998; Metzger 2019). The composition of heavy elements synthesized via the *r*-process determines the emergent spectrum. High-opacity lanthanides from neutron-rich material (electron fraction $Y_e \lesssim 0.3$) give rise to a red component, while material with higher electron fraction produces a blue component (Barnes & Kasen 2013; Kasen, Badnell & Barnes 2013; Kasen, Fernández & Metzger 2015; Kasen et al. 2017; Tanaka et al. 2017; Wollaeger et al. 2018). Tidal ejecta are dominated by neutron-rich material while disc winds exhibit a broad range of Y_e, and are thus able to support both a blue and a red component (Kasen et al. 2017; Miller et al. 2019). The blue component can be enhanced if the remnant of a BNS merger is a long-lived hyper/supramassive neutron star (Piro et al. 2019). In this case the strong neutrino irradiation would increase the electron fraction of the polar components of the ejecta, i.e. the wind from the disc and the shock-driven dynamical ejecta (Sekiguchi et al. 2016; Shibata et al. 2017; Miller et al. 2019). The blue component of an NSBH kilonova could thus be dimmer in comparison to that from a BNS merger as GW170817 (Barbieri et al. 2020b).

The presence of an EM counterpart in an NSBH is primarily dependent upon the amount of mass left outside the merger remnant, that in turn depends on the equation of state (EOS) of the NS, the mass and spin of the BH, and the orbital characteristics of the encounter (Lee & Ramirez-Ruiz 2007; Shibata & Uryu 2007; Etienne et al. 2009; Lee, Ramirez-Ruiz & van de Ven 2010; Ruffert & Janka 2010; Pannarale, Tonita & Rezzolla 2011; Shibata & Taniguchi 2011; Tanaka et al. 2014; Kawaguchi et al. 2015; Rosswog et al. 2017; Foucart, Hinderer & Nissanke 2018; Fernández, Foucart & Lippuner 2020; Krüger & Foucart 2020). These parameters drive the fraction of the NS material that is tidally disrupted and that remains outside the innermost stable circular orbit (ISCO) of the BH. The total mass of ejecta decreases with increasing BH mass, lower spin, and stiffer EOS and drops abruptly to zero once the tidal radius becomes smaller than the BH event horizon. If the NS is tidally disrupted within the ISCO, then no observable signal is expected, contrary to the BNS scenario where a kilonova accompanies mergers of all parameters.

Some numerical studies differentiated from the tidally ejected mass and the disc formed around the BH, a fraction of which produces wind ejecta (Kawaguchi et al. 2015; Fernández et al. 2020; Krüger & Foucart 2020). Others published only the total mass not immediately incorporated into the BH (Etienne et al. 2009; Ruffert & Janka 2010; Pannarale et al. 2011; Tanaka et al. 2014). These results typically agree that, if the BH is not spinning, the total mass outside the remnant BH ranges from roughly 0.1–0.2 $M_\odot$ for a 4 $M_\odot$ BH to 0.01 $M_\odot$ for a 7 $M_\odot$ BH. Most of this mass ($\gtrsim$60 per cent) forms an accretion disc, dynamical ejecta being about 10–20 per cent of this total, and wind outflows being typically 10–30 per cent of the disc mass (Metzger 2019; Miller et al. 2019). In comparison for GW170817 the mass associated to the red component, i.e. produced by the low Y_e ejecta, was estimated $\approx$0.04 $M_\odot$ (Kasen et al. 2017). In addition to these parameters, the velocity of the various components and other geometrical factors, such as the viewing angle or the shape of dynamical ejecta and the wind, determine the strength and evolution of the various EM components.

In this study, we present our search for possible optical and near-infrared counterparts of GW190814. Our campaign encompassed wide-field observations with the Deca-Degree Optical Transient Imager (DDOTI), targeted galaxy observations with the Lowell Discovery Telescope (LDT), photometric and spectroscopic follow up observations of selected candidates with the Reionization and Transients InfraRed (RATIR) and the Gran Telescopio Canarias (GTC) telescopes, respectively. In Section 2, we describe the observations and data analysis. In Section 3, we present the results of our analysis and discuss them in the context of GRB afterglows along with kilonova data in Section 4. We present our conclusions in Section 5. We note that our calculations are based on the LALInference distance estimate of 267 Mpc which falls within the 90 per cent confidence interval for the median distance reported in Abbott et al. (2020d). Reported photometry values are corrected for the estimated Galactic extinction (Schlafly & Finkbeiner 2011). Uncertainties are quoted at the 1-σ confidence level for each parameter of interest and upper limits are given at a 2-σ level, unless stated otherwise. Standard ΛCDM cosmology (Planck Collaboration et al. 2020) was adopted throughout the paper.

2 OBSERVATIONS

Follow-up observations for possible counterparts to a GW signal follow two general strategies: wide-field imaging of the GW localization area and galaxy-targeted follow-up observations. In the former case, wide-field imagers are used to perform surveys of the localization region associated with the signal. In the latter case, using a catalogue (see Bilicki et al. 2013; Dálya et al. 2018), galaxies in the 90 per cent localization volume are identified and prioritized based on their probability of hosting the merger. Photometric observations of the selected galaxies are then performed to identify transients possibly associated with the GW candidate signal (See Gomez et al. 2019; Ackley et al. 2020). The results of this strategy are affected by the completeness of the galaxy catalogue and the fraction of the total luminosity that is covered.

After this first step, transient sources showing suitable photometric evolution are identified (for example, Andreoni et al. 2020; Watson et al. 2020) and flagged for further observations. This is particularly important to rule out transients like supernovae, which are major contaminants in GW follow-up searches (see Cowperthwaite &

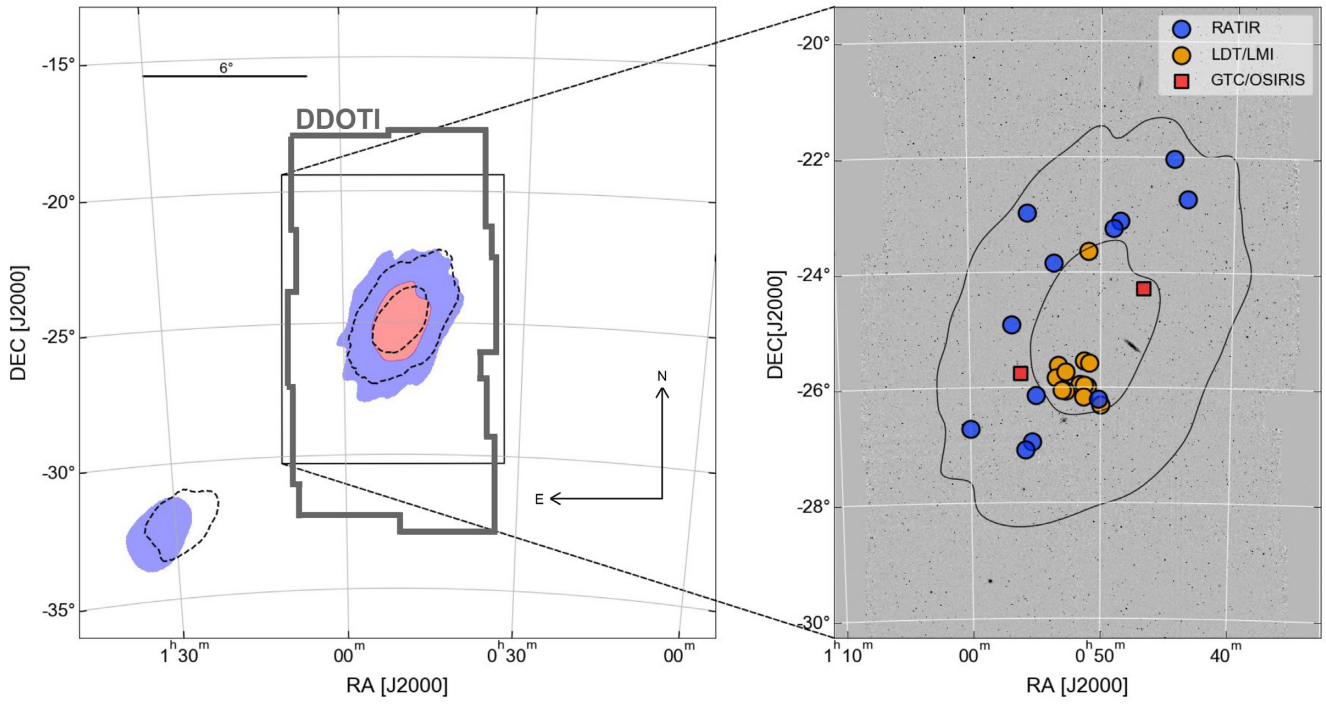

Figure 1. Left-hand panel: LALInference skymap for GW190814. The coloured contours show the 50 per cent (red) and the 90 per cent (purple) probability regions. The dashed line shows the refined localization from Abbott et al. (2020d). The area observed by DDOTI is also shown (thick line). Right-hand panel: DDOTI image of the field of GW190814. The targets observed with RATIR (blue), LDT/LMI (orange), and GTC/OSIRIS (red) are shown. The 50 per cent and 90 per cent localization areas of the LALInference skymap are superimposed on the image for reference.

Berger 2015; Doctor et al. 2017; Ackley et al. 2020; Andreoni et al. 2020). While spectroscopic follow-up can rapidly determine the distance scale and classify the origin of a transient with a higher degree of certainty, photometric observations can more easily follow a larger number of candidate counterparts.

We present wide-field observations from DDOTI in Section 2.1, galaxy targeted observations from LDT in Section 2.2, candidate targeted multicolour photometric observations from RATIR in Section 2.3, and spectroscopic observations from GTC in Section 2.4.

2.1 DDOTI wide-field imaging

The Deca-Degree Optical Transient Imager (DDOTI) employs six 28-cm telescopes with prime focus CCDs mounted on a common equatorial mount. An instantaneous field of view of 69 $\deg^2$ is obtained by adding together the six field of view of $3.4 \times 3.4\,\deg^2$ on a sky grid of 2×3 (Watson et al. 2016). DDOTI started to observe the main probability region of the updated skymap (LVC 2019b) on 2019 August 15 at 7:58 UTC, 10.8 h after the merger (Dichiara et al. 2019). The total observed field covers 88 per cent of the probability in the updated LALInference map (Fig. 1). This value does not change for the updated skymap in Abbott et al. (2020d).

Observations were taken with the airmass ranging between 1.9 and 2.8, a 100 per cent moon illumination and exposure times between 1020 and 2820 s. DDOTI images are unfiltered and photometry measurements are referred to the natural w band. In our images the number of independent elements inside the 90 per cent probability area (23 $\deg^2$) is $\approx 7.8 \times 10^6$, which sets a minimum detection threshold of 6σ for a 99 per cent confidence level. When a reference frame is available, we use this threshold for the analysis of the subtracted image. Otherwise, when comparing our source list to existing catalogues, we follow Watson et al. (2020) and adopt a 10-σ threshold to filter candidates. We present the results of this analysis in Table 1.

Table 1. DDOTI observations.

Observation Date	Mid-time (UT)	$w_{\rm max}$ (10-σ)	$w_{\rm max}$(6-σ)
15 August	09:55	18.5	19.0
16 August	09:50	18.8	19.3
18 August	09:50	18.6	19.1
21 August	09:30	19.9	–

Note. Column 1: Date of observation; Column 2: Midtime of observation; Column 3: 10-σ limit; Column 4: Reference image subtracted 6-σ limit.

Images from the first night of observations (August 15) were compared with catalogues (USNO-B1 or APASS; Monet et al. 2003; Henden et al. 2018), and no potential counterpart was found down to a limiting magnitude of $w_{\rm max} \sim 18$ AB mag (10σ; Watson et al. 2020). Additional observations of the field were carried out during the following nights (August 16, 18, and 21) using longer exposures (up to 7560 s) and reaching deeper field limits of about $w_{\rm max} = 19.9$ AB mag (10σ).

This work improves upon previous results from the first night of DDOTI observations (Dichiara et al. 2019; Watson et al. 2020) as it includes later epochs of observations (August 16, 18, and 21) which were not presented by Watson et al. (2020). We also used an updated reduction pipeline performing image subtraction and point spread function (PSF) fitting photometry instead of aperture photometry. These changes improve our sensitivity to transient sources by $\approx$1 mag with respect to Watson et al. (2020). We used the last epoch image (taken on August 21) as template to perform image subtraction on the first night of observations. After excluding fast-moving Solar system objects and image artefacts, no reliable transient was found in the

Table 2. LDT galaxy-targeted observations.

Galaxy name	R.A. (J2000)	Dec. (J2000)	Dist. (Mpc)	M_B	M_K	Upper limit (PS1 subtracted) (AB mag)	Upper limit (LDT subtracted) (AB mag)	Probability
HyperLEDA-776957	00:53:14.256	−25:36:49.68	133.2	−19.30	−20.53	21.0	21.5	0.0002
HyperLEDA-3235498	00:51:17.208	−25:32:01.32	329.6	−19.46	−23.11	21.4	21.5	0.0017
HyperLEDA-777373	00:50:52.416	−25:34:37.56	226.3	−19.46	−21.35	22.7	22.5	0.0035
HyperLEDA-3235862	00:53:24.864	−25:49:36.48	260.3	−19.51	−23.71	21.5	21.4	0.0037
HyperLEDA-3235913	00:51:36.648	−25:56:31.92	261.5	−19.36	−23.57	20.9	22.2	0.0033
HyperLEDA-772937	00:51:03.456	−25:58:56.64	304.8	−19.18	–	21.5	21.3	0.0018
HyperLEDA-773149	00:51:15.768	−25:57:39.24	300.6	−19.53	−22.53	21.7	22.0	0.0027
HyperLEDA-3235869	00:52:54.792	−26:02:28.68	334.2	−19.30	−23.41	21.2	21.3	0.0009
HyperLEDA-771948	00:52:41.880	−26:04:04.08	307.6	−19.37	−21.73	22.3	21.6	0.0019
HyperLEDA-3235867	00:52:59.016	−26:03:03.60	302.0	−19.43	−23.05	22.5	21.3	0.0021
HyperLEDA-3235948	00:50:01.104	−26:18:07.20	328.1	−19.22	−22.74	20.9	22.0	0.0008
ESO474-035	00:52:41.582	−25:44:01.87	271.4	−20.92	−24.67	22.3	–	0.0152
HyperLEDA-798818	00:50:54.447	−23:37:54.79	316.8	−21.17	−23.79	21.5	–	0.0056
HyperLEDA-2998	00:51:18.760	−26:10:05.02	285.6	−20.95	−24.14	21.8	–	0.0106

Note. Column 1: Galaxy name as indicated in the HyperLEDA catalogue; Columns 2 and 3: Galaxy coordinates; Column 4: distance as reported in the GLADE catalogue; Column 5: absolute magnitude in the *B*-band; Column 6: absolute magnitude in the *K*-band; Column 7: 95 percent *r*-band upper limits derived from the subtraction of PS1 template images. Column 8: 95 per cent *r*-band upper limits derived from the subtraction of LDT template images collected on the second epoch of observation (August 8, 18). Column 9: luminosity-weighted localization probability (see Section 2.2).

residual images down to a 6σ limit of $w_{\rm max} \approx$19 AB mag (this roughly corresponds to a 2-σ limits post trial, taking into account the number of independent elements in the field). This limit is ≈0.7 mag lower for objects in the inner regions of bright galaxies where the bright galaxy's light decreases our sensitivity to point source detection.

The time-gap between the observation of the science and template image is only 6 d. Whereas a rapidly fading kilonova such as AT2017gfo ($\Delta m_i \approx$ 2.7 mag between 10 h and 6 d from the merger; Drout et al. 2017; Pian et al. 2017; Smartt et al. 2017; Troja et al. 2017) would be detected in our observations, we are not sensitive to slowly evolving transients, such as old supernovae (SNe). For example, the bright candidate SN2019mbq ($i \sim$18.7 AB mag; Nordin et al. 2019) is not detected in the subtracted image as its magnitude is nearly constant ($\Delta m \lesssim$ 0.1 mag) between our two epochs. The other bright candidate AT2019nqr (desgw-190814d; $i \sim$18.3 AB mag) reported by Herner et al. (2019) and later classified as a type II SN (Tucker et al. 2019), lies outside the field observed with DDOTI. All the other reported candidates are fainter than our limits. Therefore, the lack of candidates in DDOTI observations is consistent with the results reported by other wide-field surveys (e.g. Ackley et al. 2020; Andreoni et al. 2020).

2.2 LDT galaxy-targeted search

We used `ligo.skymap`[2] to cross-match the LALInference map distributed by the LIGO and Virgo Collaboration (LVC) (LVC 2019a) to the Galaxy List for the Advanced Detector Era (GLADE) v2.3 catalogue (Dálya et al. 2018). A total of 806 (98) galaxies are identified inside the 90 per cent (50 per cent) probability volume. We targeted 14 of these galaxies, listed in Table 2, ranked according to the GW skymap probability, the *B*-band magnitude and the observability.

Images were obtained using the Large Monolithic Imager (LMI) mounted on the 4.3 m Lowell Discovery Telescope (LDT) on two different nights: 2019 August, 16 and 18 (1.54 and 3.54 d after the merger). The average airmass during the first night of observations was 2 and the seeing ranged between 1.78 and 1.95. On the second night the airmass varied between 2 and 2.2 and the seeing improved to values of 1.1–1.3. We observed each galaxy field taking three exposures of 90 s in the *i*-band, reaching a total exposure of 270 s and an upper limit of $i >$ 22.9 AB mag in the field. The frames collected at different epochs were used to perform image subtraction and test the possible presence of variable sources (see Fig. 2). Since the two images were acquired at similar epochs, our analysis is not sensitive to slowly evolving transients. Therefore, we also performed

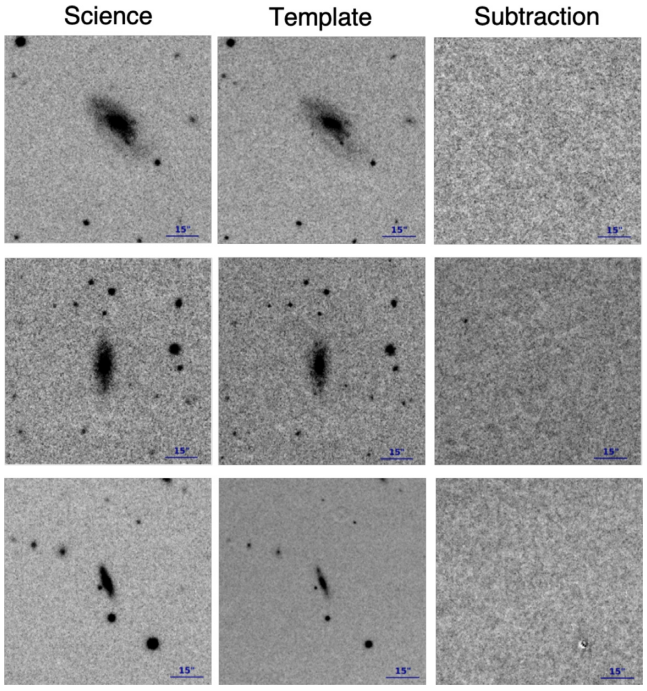

Figure 2. Example of galaxies targeted with LDT/LMI: HyperLEDA 776957 (top), HyperLEDA 773149 (middle), and HyperLEDA 777373 (bottom). Images were taken at 1.5 d after the merger (science), 3.5 d after the merger (template), and the resulting subtraction is shown in the last column. Images are 3.2 × 3.2 arcmin oriented with North up and East to the left.

[2]https://lscsoft.docs.ligo.org/ligo.skymap/

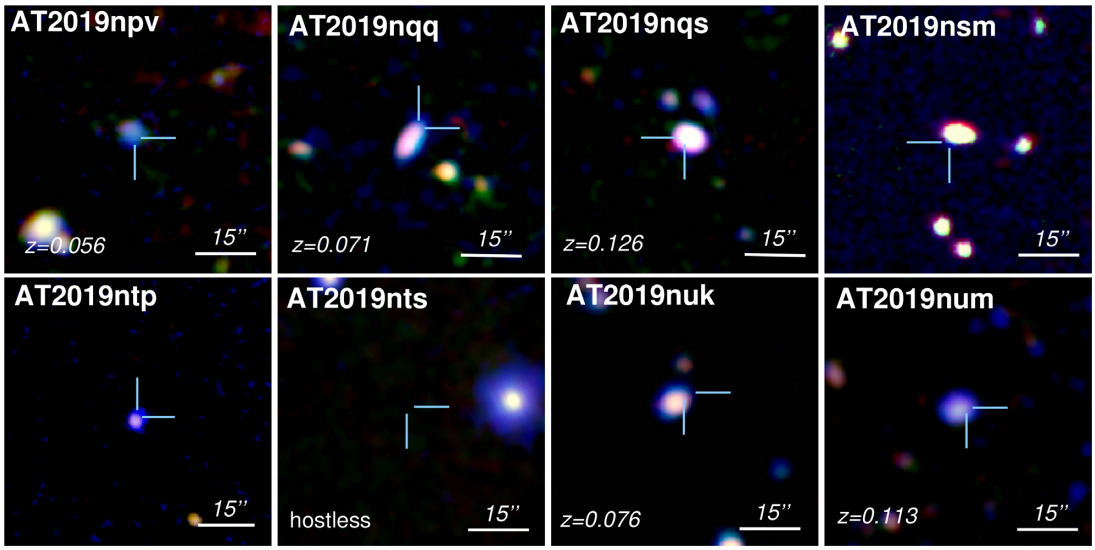

Figure 3. Candidate counterparts of GW190814 observed with the RATIR camera in different filters (*r*: blue, *Z*: green, *J*: red). All images are 1.1 ×1.1 arcmin, and are oriented with North up and East to the left. We did not detect any of the candidates in these observations, upper limits are listed in Table 3.

image subtraction using the Panoramic Survey Telescope and Rapid Response System (Pan-STARRS) 3π survey images (PS1; Chambers et al. 2016) as a template. No transient is detected in any of the targeted galaxies. Derived upper limits are reported in Table 2.

For each galaxy, we estimated the probability of hosting the NSBH merger by weighting the 3D localization probability density (Singer et al. 2016) for the galaxy's *B*-band luminosity (Gehrels et al. 2016). We selected galaxies brighter than $L_B > 0.1L_B^*$, where $L_B^* \approx 1.2 \times 10^{10}\ h^{-2}\ L_{B,\odot}$ is the characteristic galaxy luminosity of the Schechter function (Schechter 1976), and $h = H_0\ /\ (100\,\mathrm{km\,s^{-1}\,Mpc^{-1}}) \sim 0.7$ (Freedman et al. 2020). Similar to Ackley et al. (2020), our computation takes into account that the sample of GLADE galaxies inside the 90 per cent probability volume is ≈80 per cent complete in terms of integrated B luminosity. Our values therefore may differ from those reported by HOGWARTs (Salmon et al. 2020), which follows different galaxy's selection criteria and does not include the catalogue's completeness. Summing together the contribution of all the LDT galaxies we obtain a combined probability of ≈5 per cent, although it is difficult to make strong probabilistic statements due to the uncertainty on GLADE completeness.

Although our observations cover a small fraction of the possible galaxies, our analysis provides an independent confirmation for the lack of candidates and it includes three galaxies not covered by other searches reported in the literature (e.g. Gomez et al. 2019; Ackley et al. 2020; Vieira et al. 2020): HyperLEDA 776957, HyperLEDA 3235869, and HyperLEDA 3235948.

2.3 RATIR follow-up

While our DDOTI and LDT observations focused on the search of candidate counterparts, we used the 6-filter imaging camera RATIR (Butler et al. 2012; Watson et al. 2012) to monitor the sources reported by other collaborations. Sixteen candidates discovered in the Dark Energy Camera (DECam) images and reported by the DECam-GROWTH team (Andreoni et al. 2020) and DECam-DESGW team (Herner et al. 2019) were observed using RATIR (Fig. 3).

Observations started on August 19 (about 4.4 d after the merger) obtaining simultaneous photometry of the candidates in *riZJ* and *riYH* filters. Additional observations were collected between August, 20 and 22 in order to characterize the sources variability, and observe newly reported candidates. Moon illumination varied from 87 per cent to 53 per cent during this period with airmass ranging between 1.7 and 3.8. The average exposure in each filter is approximately 1200 s for *r*, *i* band, approximately 500 s for *Z*, *Y*, *J*, and *H* band. The 2-σ field upper limit in the *i*-band varies between 20.8 and 22.0 AB mag. On August 28, a deep (3.8 h) *r*-band image was obtained for the radio candidate AT2019osy (Dobie et al. 2019) for which we reach a field limit $r \gtrsim 22$ AB mag.

None of the candidate counterparts were detected in our observations, the resulting upper limits are listed in Table 3. Optical limits are derived after subtracting the host galaxy light using PS1 reference frames. No reference frames were available for the nIR observations, and we therefore estimated our sensitivity by planting artificial point-like sources at the transient position. Our limiting magnitude is then determined by the faintest object detected with `Source Extractor` (Bertin & Arnouts 1996).

2.4 GTC (+OSIRIS) spectroscopy

We triggered observations of four candidate counterparts whose photometric redshifts were consistent with the distance of the GW source (Goldstein et al. 2019a): AT2019nqz (Goldstein et al. 2019a), AT2019nqc, AT2019nqq (Herner et al. 2019), AT2019npw (Andreoni et al. 2019). These observations were performed using the Optical System for Imaging and low-Intermediate-Resolution Integrated Spectroscopy (OSIRIS; Cepa et al. 2000) spectrograph mounted on the 10.4 m Gran Telescopio de Canarias (GTC). The four object spectra were obtained using the R300R grism, covering a wavelength range of 5000–10 000 Å. However, we find calibration issues between 9000 and 10 000 Å, so our analysis is restricted to the wavelength range 5000–9000 Å. The observations obtained with GTC(+OSIRIS) are detailed in Table 4.

The spectra have been reduced using standard procedures under `IRAF/PyRAF` (Tody 1986). They were bias subtracted and corrected for flat-field. Then, we computed for each frame a wavelength solution using an iterative method, based on previous line identifications, and applied to the observation night's lamp frames. Flux

Table 3. RATIR observations of candidate counterparts.

Candidate	R.A. (J2000)	Dec. (J2000)	Date	m_i (AB mag)	m_J (AB mag)	Redshift	Spectral classification
AT2019npv	00:53:32.316	−23:49:58.51	2019-08-19	21.0	19.2	0.056	SN Ib
AT2019ntp	00:50:12.072	−26:11:52.56	2019-08-19	21.2	19.1	–	SN Ic
AT2019nsm	00:43:30.160	−22:43:29.35	2019-08-20	21.6	18.9	–	–
AT2019ntr	01:00:01.884	−26:42:51.59	2019-08-19	21.5	19.8	0.2	SN II
AT2019nts	00:48:31.441	−23:06:40.80	2019-08-19	21.0	19.4	–	–
AT2019ntn	01:34:53.349	−31:22:49.75	2019-08-20	21.3	18.5	0.1	SN[a]
AT2019nuj	00:49:01.738	−23:14:04.93	2019-08-19	21.1	19.7	0.074[c]	–
AT2019nuk	00:54:57.827	−26:08:04.61	2019-08-21	20.8	18.4	0.076	–
AT2019nul	00:55:16.443	−26:56:34.57	2019-08-20	20.8	18.7	0.098	–
AT2019num	00:55:31.603	−22:58:08.48	2019-08-20	20.9	19.2	0.113	SN II
AT2019nun	00:56:48.599	−24:54:30.48	2019-08-21	21.3	18.7	0.131	–
AT2019nus	00:44:34.557	−22:01:44.62	2019-08-21	21.7	19.9	–	–
AT2019nqc	01:29:03.669	−32:42:18.56	2019-08-22	20.6	19.8	0.078	SN IIP
AT2019nqs	01:33:35.164	−31:46:48.48	2019-08-20	21.3	18.2	0.1263	SN[a]
AT2019nqq	01:23:49.217	−33:02:04.99	2019-08-20	19.5	20.0	0.071	SN Ic
AT2019osy	00:55:47.400	−27:04:32.99	2019-08-28	22.0[b]	–	–	AGN

Notes. Column 1: source identifier; Columns 2 and 3: source coordinates; Column 4: observing date; Column 5: 95 per cent *i*-band upper limit; Column 6: 95 per cent *J*-band upper limit; Column 7: measured redshift; Column 8: source classification derived from this work (see Section 3.2), Andreoni et al. (2020), Ackley et al. (2020) and from Dobie et al. (2019) for AT2019osy.
[a]Uncertain type.
[b]95 per cent *r*-band upper limit.
[c]Photometric redshift of the host galaxy

Table 4. GTC observations log.

Source	RA (J2000)	Dec (J2000)	Obs. date	Exp. time	Grism	Slit width (arcsec)	Airmass	Seeing (arcsec)
AT2019npw	00:56:05.742	−25:45:01.58	2019-08-19	1×1200 s	R300R	1.23	1.78	1.6
AT2019nqq	01:23:57.720	−33:05:14.89	2019-08-19	1×1200 s	R300R	1.23	2.11	2.5
AT2019nqc	01:29:03.479	−32:45:53.50	2019-08-20	3×400 s	R300R	1.23	2.08	1.8
AT2019nqz	00:46:47.397	−24:16:32.26	2019-08-20	3×400 s	R300R	1.23	1.66	1.3

calibration was performed using standard star observations taken on the same night. The calibrated images were cosmic ray subtracted using `ccdproc` (Craig et al. 2017) after which the spectra were extracted from the individual calibrated science images and then combined. After extraction of the spectrum for each of the objects, we smoothed the spectrum using a Gaussian kernel to better identify broad absorption features.

We estimate the redshift of the host galaxy for each object by identifying the strongest narrow emission features in the spectrum, and assuming that they come from H II regions of the galaxy. After constraining the redshift, we investigated whether the observed spectra originate from a kilonova associated with GW190814.

An important step for identifying a transient as a counterpart to a GW event is to confidently reject possible alternative origins, in particular SNe, which are a major source of contamination (e.g. Cowperthwaite & Berger 2015; Doctor et al. 2017; Ackley et al. 2020; Andreoni et al. 2020).

We therefore looked for SN signatures by visual inspection, as well as by matching template spectra using SNID (Blondin & Tonry 2007). For further support to our findings, we also measured the blueshift of the SN features in the reference frame of the host galaxy. We list the features that we identify and the blueshift velocities that we measure for them in Table 5. We also compared our values with the results by Liu & Modjaz (2014), Modjaz et al. (2016), and Liu et al. (2016) and we report the expected mean values for the blueshift velocities in Table 5. The results of this analysis are elaborated in Section 3.2.

3 RESULTS

3.1 Photometric classification of candidates

In the days following the candidate signal GW190814, over 70 candidates were proposed through GRB Circular Notice[3] (GCN), the majority with discovery magnitude fainter than $\gtrsim$21 AB in the optical. A rapid spectroscopic identification for such large number of sources is not feasible, and multicolour imaging could more easily aid in their classification (e.g. Golkhou et al. 2018). For GW190814 most of the candidates were already faint at discovery and, also due to the poor observing conditions (high airmass and moon illumination), RATIR observations did not have sufficient sensitivity to follow their temporal and spectral evolution. They can however exclude the presence of a rising light curve, typical of an off-axis afterglow (Granot et al. 2002; Ryan et al. 2020).

Better constraints are possible for candidates brighter than $\lesssim$20 AB mag at discovery time. Their temporal evolution is shown in Fig. 4. The brightest candidate observed with RATIR is AT2019nuk. The source, first detected with $i\sim$19.02 AB mag at 2 d, dropped to $\sim$21.6 AB mag at 3.5 d and was not detected in our observations, confirming its rapid fading. Spectroscopic observations of the host galaxy place it at $z = 0.076$ (Ackley et al. 2020), consistent with the GW distance scale. The observed temporal decay is steeper than

[3]https://gcn.gsfc.nasa.gov/other/GW190814bv.gcn3

Table 5. GTC/OSIRIS analysis results.

Candidate	Element (Ion)	Expansion velocity	Expected mean velocity
AT2019nqz (SNIIb)	Hydrogen (H I)	$-16\,000$ km s^{-1}	$-12\,000$ km s^{-1} [a]
	Helium (He I)	$-12\,000$ km s^{-1}	-8000 km s^{-1} [a]
AT2019nqq (SNIc)	Oxygen (O I)	-4000 km s^{-1}	-9000 km s^{-1} [a]
	Silicon (Si II)	-4000 km s^{-1}	-9000 km s^{-1} [b,c]
AT2019nqc (SNIIP)	Hydrogen (H I)	-6000 km s^{-1}	$-12\,000$ km s^{-1} [a,c]
	Helium (He I)	-6000 km s^{-1}	-8000 km s^{-1} [a]
AT2019npw (SNIIb)	Hydrogen (H I)	$-10\,000$ km s^{-1}	$-12\,000$ km s^{-1} [a,c]

Notes. Column 1: Transient name and its classification; Column 2: Line features identified; Column 3: Blueshift velocity in the reference frame of the host as measured in our analysis; Column 4: Mean expected velocity obtained from the literature.
[a]Liu et al. (2016).
[b]Modjaz et al. (2016).
[c]Gal-Yam (2017).

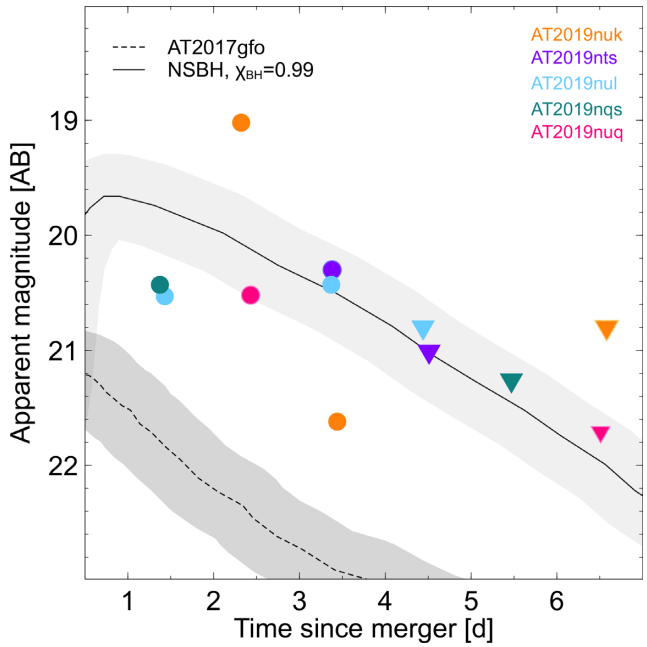

Figure 4. Temporal evolution of the brightest candidate counterparts observed with RATIR. RATIR *i*-band upper limits are marked as downward triangles. Other optical observations (marked as filled circles) were retrieved from the Transient Name Server (TNS)[4]. The dashed line shows the evolution of AT2017gfo (using data from Troja et al. 2017) shifted to 270 Mpc. The solid line shows the NSBH model from Barbieri et al. (2020a) for a maximally spinning BH, also shifted to 270 Mpc. The shaded areas reflect the $1\,\sigma$ uncertainty in the source distance scale.

the decay rate observed in AT2017gfo or, in general, predicted by kilonova models at a similar epoch. A sharp drop in the UV flux was observed in the early phases of AT2017gfo (Evans et al. 2017), with the peak of the emission shifting towards redder wavelengths. In the case of AT2019nuk, if a rapid spectral evolution was at the origin of the optical decay, we should see its bright peak moving towards the nIR bands. As the source remains undetected at all wavelengths (see the optical and nIR upper limits in Table 3), we conclude that multicolour photometry disfavours a kilonova classification. Furthermore, at a distance of $z = 0.076{\sim}345$ Mpc, the source brightness ($M \approx -18.7$ mag at 2 d) exceeds the expected emission from a radioactive-powered kilonova, whereas it falls within the distribution of short GRB optical afterglows. The rapid decay of the light curve is atypical for an afterglow too, although not unprecedented. For example, Piranomonte et al. (2008) observed a similar fast decay rate $f_{\rm opt} \approx t^{-5.3\pm0.9}$ for the short GRB 070707. Therefore, based solely on the optical/nIR follow-up, we could not unambiguously rule out the hypothesis of a (peculiar) on-axis GRB afterglow for AT2019nuk. The strongest constraint in this sense comes from the lack of a bright gamma-ray burst, ruled out by *Swift* observations at the time of the merger (Palmer et al. 2019), as well as from our wide-field DDOTI observations (Section 4.2).

A similar argument applies to AT2019nts, observed to fade from $i \sim 20.3$ AB mag at 4 d (Goldstein et al. 2019b) to $i > 21$ AB mag at 5 d, which implies a decay slope $\gtrsim$2. The source lies $\approx$30 arcsec East from a bright galaxy (Fig. 3), whose redshift is not known. By assuming the same distance of GW190814, its luminosity and decay rate would be consistent with a post jet-break GRB afterglow, while a kilonova origin appears again unlikely due to the lack of detection in the redder filters. The hypothesis of an on-axis GRB is however not supported by the gamma-ray and wide-field optical data. Assuming a typical afterglow decay rate to extrapolate their magnitudes back in time, both AT2019nuk and AT2019nts would have been detectable during the first night of DDOTI observations.

Another bright candidate is AT2019nul, with a discovery magnitude of $i \sim 20.4$ AB. Over the first few nights of observation, the source shows a slow temporal evolution (Andreoni et al. 2020) as well as a rather shallow spectral index, as suggested from our lack of detection in the nIR bands. These properties differ from both kilonova and afterglow counterparts. Spectroscopic observations later published in Ackley et al. (2020) place this object at $z = 0.098$, outside the 99 per cent probability volume of the GW source, confirming that this transient is unrelated to the merger.

The last bright candidate followed with RATIR is AT2019nqs. It was discovered on August 16 (2 d post-merger) with magnitudes of $z = 19.69$ and $i = 20.43$ (AB). RATIR observations do not detect the source, which is close to its galaxy's centre (Fig. 3), and derive a limit of $i > 21.3$ AB mag at 4 d. This candidate was rapidly discarded by spectroscopic follow-up (Bruun et al. 2019; Ackley et al. 2020), which placed it at a distance of $z = 0.126$ (about 600 Mpc), well beyond the GW distance range, and tentatively identified it as a Type I SN.

For this GW event, the average sensitivity of RATIR observations ($m_i \lesssim 21$ AB mag) is comparable to the peak magnitude of a AT2017gfo-like kilonova at $\approx$270 Mpc (see Fig. 4). Therefore, they

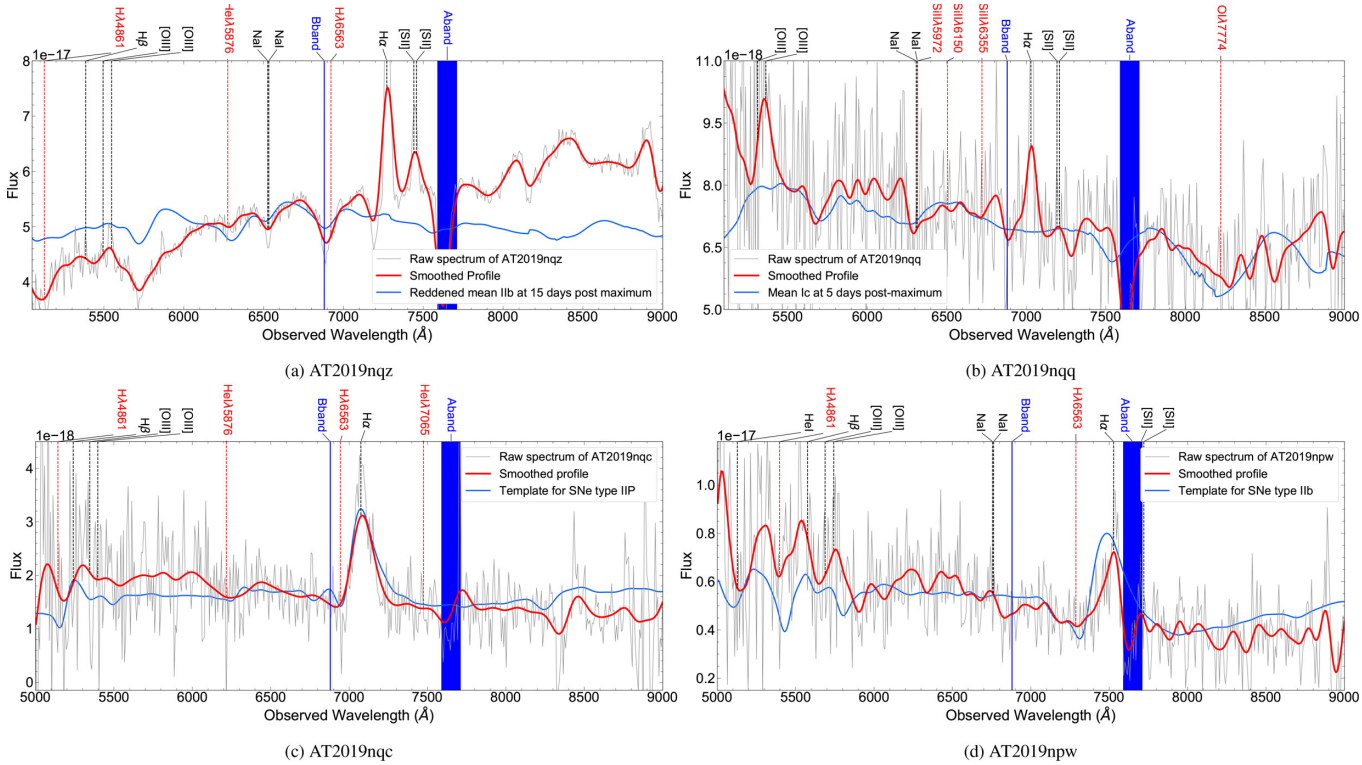

Figure 5. OSIRIS spectra of AT2019nqz, AT2019nqq, AT2019nqc, and AT2019npw. The GTC/OSIRIS spectrum is plotted in grey. We overplot the smoothed profile of the spectrum (red) to emphasize broad absorption features. For comparison, we also plot SNe templates obtained from the literature at the redshift of the host (blue). We mark host galaxy line features in black and the telluric bands in blue. We mark broad transient line features for which we observe a good match with the template in red.

cannot exclude the presence of an event of similar brightness. An NSBH merger involving a non-spinning BH ($\chi_{\rm BH} = 0$) or a NS with a soft equation of state (EoS) would also produce a faint signal (Barbieri et al. 2020b), and could not be constrained. Our observations are instead sensitive to the brightest kilonova predictions from Barbieri et al. (2020b), calculated for an NSBH merger with chirp mass $\approx$1.4 $M_\odot$, a stiff NS equation of state (EoS; Typel et al. 2010) and maximal BH spin $\chi_{\rm BH} = 0.99$. These values differ from those derived by the analysis of the GW signal, nevertheless our comparison shows that for events at $\gtrsim$200 Mpc a range of merger properties could still be probed by the EM observations. Preliminary indications on the mass ratio and orientation of the merging binary would be a critical input in order to effectively target the most promising systems.

3.2 GTC(+OSIRIS) spectral analysis results

3.2.1 AT2019nqz

The AT2019nqz spectrum (Fig. 5a) shows a red continuum. It has a prominent and sharp Hα emission at $\sim$7273 Å and a sharp [S II] feature at $\sim$7448 Å. This identification is also supported by the presence of Hβ at $\sim$5389 Å and [O III] emission lines at $\sim$5550 Å. We determine a redshift value of $z = 0.108$ for the host spectrum using the emission features detailed above, consistent with the preliminary analysis reported in Lopez-Cruz et al. (2019, $z = 0.1076$). This is outside the redshift range allowed by the LVC localization, and therefore unrelated to the GW source. Nonetheless, we also attempt to classify the transient in order to better characterize the contaminants of the GW follow-up. Lopez-Cruz et al. (2019) also report that the transient appears to be closer than 0.5 arcsec from the host. Using our low quality acquisition images obtained by GTC, we confirm that there is no evident point source distinguishable on or near the host galaxy.

The [O III] and Hβ features in the spectrum are clearly weaker than [S II] and Hα. This, in conjunction with the red continuum, suggests that the line of sight is strongly obscured. We confirm this by following Calzetti, Kinney & Storchi-Bergmann (1994), Calzetti et al. (2000), Osterbrock (1989), and computing the Balmer decrement from the measurement of the emission line fluxes. Assuming that

$$E(B-V) = 1.97 \log \frac{(\mathrm{H}\alpha/\mathrm{H}\beta)_{\rm obs}}{2.86}, \quad (1)$$

we obtain $E(B-V) \sim 1$.

In order to classify the type of galaxy, and given that both AGNs and star forming galaxies are characterized by strong and narrow emission lines, we use the Baldwin–Phillips–Terlevich (BPT; Baldwin, Phillips & Terlevich 1981) method to discern the nature of this galaxy. As we cannot measure [N II] and [O I] fluxes from our spectrum, we can only apply the BPT-SII diagnostic (see Kewley et al. 2006, and references therein). We find that

$$\log \frac{[\mathrm{O\ III}]}{\mathrm{H}\beta} \approx \frac{0.72}{\log \frac{[\mathrm{S\ II}]}{\mathrm{H}\alpha} - 0.32} + 1.30, \quad (2)$$

which places this galaxy on the limit between AGNs and star forming galaxies and thus cannot break the degeneracy between the two possible classifications. Therefore, as we cannot identify any point source on or near the galaxy, we cannot completely reject the possibility that this transient can be due to nuclear activity.

However, we find that the broad absorption lines observed in the spectrum can be better explained as the superposition of SN features. We can explain the broad peaked blue absorption feature at ∼6926 Å next to the host's H α emission as a blending of H α absorption from the SN and the atmospheric *B*-band; with possible contribution from the host as well. We can then associate the bluest absorption at ∼5123 Å to H β absorption from the SN. This is further supported by the good match of the observed absorption features with the average spectrum of a type IIb SN at 15 d post maximum obtained by Modjaz et al. (2016, see Fig. 5a). Therefore, based on these identifications and the velocities we measure (Table 5), we find that there is also a type II supernova in the line of sight to AT2019nqz.

The EW of the Na I doublet is commonly used to infer the extinction in the line of sight to SNe (e.g. Barbon et al. 1990; Turatto, Benetti & Cappellaro 2003; de Jaeger et al. 2018) and galaxies (Poznanski, Prochaska & Bloom 2012), despite the fact that this method has known limitations (see e.g. Poznanski et al. 2011). From our spectrum, we measure a rest frame EW(Na I) = 3.97 Å. This large value is not seen in the SDSS galaxy sample collected by Poznanski et al. (2012) (we expect EW ∼0.6 Å for $E(B-V) \sim 1$ from their Fig. 8). However, our values are consistent with the relationship found for SNe as inferred from fig. 3 of Turatto et al. (2003) and fig. 1 of Poznanski et al. (2011). Therefore, the EW(Na I) value we measure from our spectrum strengthens our previous result that AT2019nqz is a type II supernova.

3.2.2 *AT2019nqq*

The AT2019nqq spectrum shows a blue continuum (Fig. 5b). We calculate a redshift of $z = 0.071$ for the host. Our result is consistent with the value reported by Andreoni et al. (2020), and places this transient within the distance range of the GW source. The host galaxy's redshift is constrained using a prominent and narrow emission line at ∼7032 Å, which we interpret as H α emission from the host. This identification is supported by the [O III] emission features at ∼5230 Å. We also marginally detect an emission feature at ∼7195 Å, which is consistent with [S II] doublet emission at the same redshift. At difference with Andreoni et al. (2020), we do not find H α emission wide enough to support their Type II SN classification. Furthermore, the apparent P-Cygni profile is most likely due to the atmospheric *B*-band.

Instead, the absence of strong hydrogen features favours a type I SN classification. We identify a weak Si II absorption feature centred at ∼6700 Å. We also identify an absorption feature centred at ∼8198 Å which is consistent with O I absorption from the SN. The combination of the weaker Si II relative to the O I feature and velocity values favours a type Ic classification (velocity values are summarized in Table 5; see Modjaz et al. 2016; Gal-Yam 2017). We overplot in Fig. 5(b) an average type Ic spectrum 5 d post maximum for comparison with our spectrum, finding a reasonable match between them, keeping in mind that our spectrum is not host-subtracted. We thus find that the AT2019nqq spectrum favours a type Ic classification.

3.2.3 *AT2019nqc*

The AT2019nqc spectrum (Fig. 5c) shows a flat continuum. The host redshift is constrained assuming that the prominent peak component at ∼7536 Å is H α coming from H II region(s) in the galaxy, at a redshift of $z \sim 0.078$, consistent with the measurement of Andreoni et al. (2020), and within the 95 per cent distance range of GW190814.

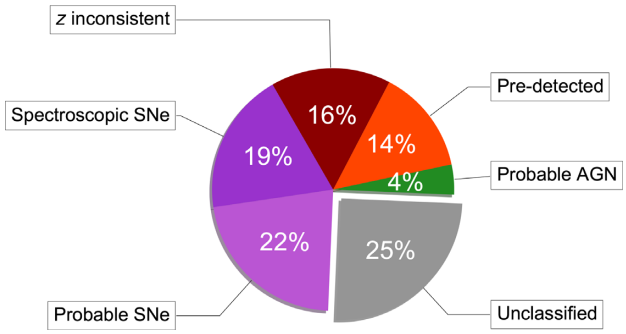

Figure 6. Classification scheme for candidate optical counterparts of GW190814. Archival detections, Solar System objects, and proper motion star are grouped under pre-detected. Sources ruled out on the basis of redshift, either photometric or spectroscopic, are combined under *z*-inconsistent. Probable SNe and probable AGNs were classified on the basis of their photometric evolution.

We do not detect convincing [O III] or H β features, suggesting that the spectrum is dominated by a transient source. This is supported by the presence of a very broad H α emission component next to a weak absorption feature. These characteristics are typical of type II SNe.

The transient spectrum has a H α P-Cygni profile. We also detect H β absorption at ∼5131 Å, and He I absorption features at ∼6223 and ∼7463 Å. We note that the feature at ∼7463 Å is very weak. These characteristics suggest a type II SN classification for this spectrum, as independently suggested by Andreoni et al. (2020). For comparison, we overplot the spectrum of the type IIP SN2005cs (Muendlein et al. 2005). The template spectrum is at 4 d post maximum.

3.2.4 *AT2019npw*

The AT2019npw spectrum (Fig. 5d) shows a blue continuum. The host redshift is constrained using the prominent H α line at ∼7536 Å and [O III] emission features at ∼5750 Å. We further identify [S II] emission at ∼7708 Å. We find the redshift of the host to be $z = 0.147$, well beyond the GW distance range.

This object has been reported by Andreoni et al. (2020) as a type IIb SN and the combination of spectral features that we identify supports this conclusion.

The transient spectrum has a clear broad H α absorption feature at ∼7297 Å. We further find H β absorption at ∼5423 Å. The velocity values we measure for this spectrum are summarized in Table 5

We plot the type IIb SN2004et (see Zwitter, Munari & Moretti 2004) as a reference spectrum for comparison. The spectrum is at 9 d post maximum. We find good agreement in the profile of our spectrum and template, which supports our classification.

4 DISCUSSION

4.1 Optical candidates follow-up campaign

A total of 85 optical transients, with brightness ranging between 18 and 24 AB mag, were identified as candidate counterparts of GW190814. Of these, 71 were announced via Gamma-ray Coordinates Network notices (GCNs) and 14 were reported at a later time through publications. Fig. 6 summarizes the results of this community wide effort. Based on the results of our analysis and other works (e.g. Ackley et al. 2020; Andreoni et al. 2020), 42 candidates can be

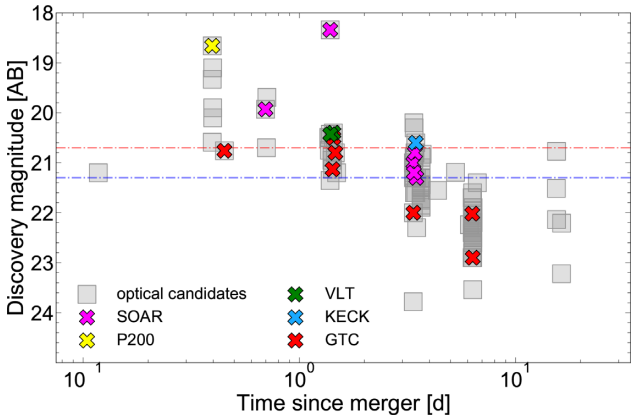

Figure 7. Discovery magnitude of optical counterpart candidates for GW190814 as a function of time. The discovery magnitudes are as obtained from GCNs. Spectroscopically classified transients are coloured differently to highlight the facilities used for the classification. The median magnitude for the entire set of 85 candidates (21.3 mag, blue) and the median magnitude for the subset of spectroscopically classified candidates (20.7 mag, red) are marked as horizontal dashed lines.

ruled out as counterparts of the GW source: 17 are spectroscopically classified, 5 have photometric redshifts inconsistent with the GW signal, 9 are associated to a host galaxy with redshift inconsistent with the GW signal, 9 have archival detections, and 2 are moving objects. This then leaves 43 candidates (∼50 per cent) without a secure classification. For these, 19 are probable SNe based on their light-curve evolution, and 3 are probable active galactic nuclei (AGNs). The remaining 21 sources (∼25 per cent) are left unclassified. Of these, 10 candidates have photometric redshifts consistent with the GW distance (within the 95 per cent uncertainties), 2 have host galaxy spectra whose redshifts are consistent with the GW distance, and 9 have no constraints on their distance scale. The magnitude of the candidates that are redshift consistent with the GW distance ranges from 23.2 to 21.3 AB mag.

We find that of the 17 spectroscopically classified candidates, one is a proper motion star and 16 are identified as SNe: 9 are Type II, 2 are Type Ibc, 2 are Type Ia and 3 have an unclear sub-type classification. Combining the number of classified SNe and probable SNe, we get a total of 35 optical candidates (≈40 per cent) that could be classified as SNe. This is consistent with the predictions that SNe are major contaminants in the optical follow-up of GW events due to their rates and luminosity (Nissanke, Kasliwal & Georgieva 2013; Cowperthwaite & Berger 2015).

We further investigate whether the results may be affected by observing biases, preferentially targeting a particular type of transient. Fig. 7 reports the discovery magnitude of all the proposed candidates as a function of their time of announcement. On average, brighter sources were reported at early times. We calculate a median discovery magnitude of 21.3 for the entire sample of candidate counterparts. The median magnitude for the subset of spectroscopically classified candidates is 20.7, only slightly brighter than the complete sample. We use the Kolmogorov–Smirnov test to compute the probability that the two sets of magnitude can be drawn from the same probability distribution finding a p-value of 0.08. Therefore, we cannot identify any significant difference between the entire set of candidates and the subset of spectroscopically classified sources.

The follow-up of candidates reported within the first 4 d was very thorough: 27 candidates were announced via GCNs, out of which 18 (∼67 per cent) have spectroscopic observations (13 with a spectroscopic classification). In a few cases (AT2019nqq, AT2019nqc, and AT2019npv) multiple spectroscopic observations were reported. For the candidates announced at later times (>4 d), we do not recognize any clear pattern in the selection criteria for spectroscopic follow-up. Instead, we note that most of these candidates remain unclassified. Therefore, time rather than brightness was the discriminant factor in obtaining a spectroscopic identification.

This factor may have been partially influenced by the behaviour of AT2017gfo, which peaked at early times and then rapidly faded at optical wavelengths. The expectation of a weak signal probably discouraged the pursuit of additional spectroscopic observations. However, a wider range of kilonova peak times and decay rate is predicted by models (see Section 4.3), and an improvement in late-time spectroscopic follow-up strategy could increase the chance of detecting kilonova signals differing from AT2017gfo. In the case of GW190814, a key factor may also have been the low probability of an EM signal, as calculated by the LVC preliminary analysis (LVC 2019b).

It is worth noting that large aperture telescopes, such as the W. M. Keck Observatory (Dimitriadis et al. 2019), the Southern African Large Telescope (SALT; Andreoni et al. 2020), the Gran Telescopio de Canarias (GTC, this work), and the Very Large Telescope (VLT; Ackley et al. 2020), played a key role in securing the spectroscopic observations.

4.2 Constraints on afterglow emission and implications for the GRB jet

We use optical limits on the GW counterpart to constrain the presence of a relativistic jet component, as observed in short gamma-ray bursts (sGRBs). In Fig. 8 (left-hand panel), we compare the optical upper limits to a sample of 21 sGRB afterglows with known redshift, rescaled to a distance of 267 Mpc (Watson et al. 2020). The presence of a typical on-axis sGRB afterglow is disfavoured by the wide-field data: limits from DDOTI rule out 60 per cent of the light curves with a coverage of 88 per cent (corresponding to a 53 per cent probability). This is an improvement over the detection probability (∼30 per cent) obtained by Watson et al. (2020), as our limit is 1 mag deeper. The constraints from DECam and VST can exclude up to 80 per cent of the cases with a coverage of 92 per cent and 61 per cent, corresponding to a probability of 70 per cent and 49 per cent, respectively.

This comparison is however based on detected sGRB afterglows, and may be biased towards the brighter end of the luminosity distribution. In order to assess our ability to constrain on-axis GRB explosions, we also ran a set of 10 000 simulations with input afterglow parameters representative of the broader sGRB population, including events without an observed optical counterpart. We adopt the standard framework of synchrotron emission from shock-accelerated electrons with an energy distribution $N(E) \propto E^{-p}$ and $p = 2.2$. Four parameters describe the afterglow behaviour: the isotropic equivalent kinetic energy (E_0), the density of the external medium (n), the fraction of energy transferred to the electrons (ϵ_e), and to the magnetic field (ϵ_B). These parameters were randomly assigned assuming the observed distributions (O'Connor, Beniamini & Kouveliotou 2020), and simulated light curves for an on-axis top-hat jet were created using `afterglowpy`[5] (Ryan et al. 2020). The jet opening angle was fixed to a fiducial value of 5° (e.g. Troja et al. 2016; Jin et al. 2018). Since the effects of collimation become apparent at $t \gtrsim 1$ d, this particular choice does not affect our

[5]https://github.com/geoffryan/afterglowpy

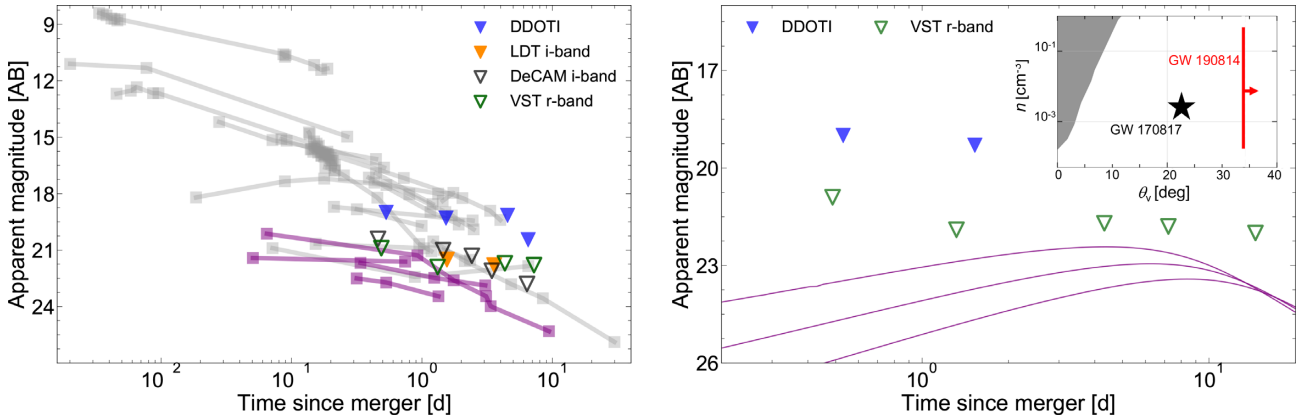

Figure 8. Left-hand panel: Optical upper limits for GW190814 in comparison to observed short GRB afterglows. The light curves are scaled to a distance of 267 Mpc. Upper limits obtained from DDOTI and LDT are marked with filled symbols (blue and orange; respectively) and the upper limits from DECam and VST are marked with empty symbols (black and darkgreen; respectively). The afterglows that cannot be ruled out are coloured purple. Right-hand panel: Optical upper limits for GW190814 in comparison to off-axis afterglow light curves, calculated using the explosion properties of GW170817 (Troja et al. 2019; Ryan et al. 2020) and viewing angles of 13°, 14°, and 16°. The inset shows the constraints on density as a function of the viewing angle. The region ruled out by the upper limits is shaded grey. The lower limit on the inclination for GW190814 is marked with a vertical red line.

conclusions, mostly driven by the early-time (≈12 h) upper limits. Based on these simulations, a sizable fraction of on-axis afterglows can be confidently ruled out: we derive a 40 per cent probability from DECam constraints, a ≈30 per cent probability from DDOTI and VST limits.

Given the low rate of sGRBs in the local Universe (e.g. Dichiara et al. 2020), the probability of intercepting an on-axis event is however very small. An off-axis explosion, that is a GRB jet not aligned to our line of sight, is a more likely counterpart of a GW source. Off-axis afterglows are much fainter than their on-axis counterparts, and could easily escape optical/nIR searches. For example, we consider the case of GW170817 and investigate whether a similar explosion could have been detected for GW190814. We use `afterglowpy` (Ryan et al. 2020) to simulate 2280 optical light curves with the same physical parameters derived for GW170817 and a range of viewing angles (θ_v) and densities (n). For typical ISM densities $n \gtrsim 10^{-4}$, the GW afterglow would have been detected if on-axis ($\theta_v = 0$). However, the detection probability drastically decreases with increasing viewing angles, and becomes negligible for $\theta_v > 10$ deg (see inset of 8). Therefore, for the range of values derived from the GW data $\theta_v = 45^{+18}_{-11}$ deg (Abbott et al. 2020d), any off-axis afterglow would have escaped detection.

4.3 Constraints on kilonova ejecta properties

Optical and infrared observations constrain properties of a possible kilonova associated with GW190814. We compare upper limit observations to simulated kilonova light curves with varying input parameters corresponding to the distribution and properties of matter outside the remnant compact object. The amount of material ejected from an NSBH binary depends on the properties of the compact objects and, in particular, the BH mass and its spin. If the BH is not spinning, the total mass outside the remnant is roughly 0.1–0.2 $M_\odot$ for a 4 $M_\odot$ BH. This total ejecta mass decreases with increasing BH mass, falling to 0.01 $M_\odot$ for a 7 $M_\odot$ BH. With corotating spins, this number increases to 0.2–0.3 $M_\odot$ for a 4 $M_\odot$ black hole (Kawaguchi et al. 2015). Typically, the dynamical ejecta masses are a factor of 5 to 10 times lower than this total, with the remainder forming an accretion disc around the remnant compact object. Wind ejecta masses are roughly 10–30 per cent of the disc mass (Miller et al. 2019). However, only BHs with masses below 5 $M_\odot$ and/or very large disc masses will produce sufficient disc outflows to sustain an observable kilonova (Fernández et al. 2020). The final parameter estimates for GW190814 correspond to the merger of a 23 $M_\odot$ black hole with a 2.6 $M_\odot$ compact object (Abbott et al. 2020d) leaving little chance for matter outside the remnant BH, and thus significantly reduce the probability of producing an observable kilonova.

By comparing observational upper limits to kilonova light-curve models, we can place independent constraints on the properties of both dynamical and wind ejecta components from this merger. Past studies of GW190814 have argued for a range of constraints. Using a constant opacity model, Andreoni et al. (2020) argued that the ejecta masses were less than 0.03–0.05 $M_\odot$. Models using a more realistic opacity description and a two-component ejecta profile have argued that the ejecta masses above 0.1 $M_\odot$ are typically ruled out and, depending upon the viewing angle, some ejecta masses as low as 0.04 $M_\odot$ can be disfavoured (Kawaguchi, Shibata & Tanaka 2020). As discussed below, our results, using a broader parameter range of morphologies and ejecta velocities, disfavour models with total ejecta masses above 0.1 $M_\odot$ and, except for slow moving dynamical ejecta models, models with dynamical ejecta masses above 0.1 $M_\odot$ are nearly all ruled out. Similarly, most models with wind mass exceeding 0.1 $M_\odot$ and wind velocities above 0.15c are also inconsistent with observations.

4.3.1 Description of models

For this study, we use a grid of two-component models from the LANL group (Wollaeger et al., in preparation). The two-components include a heavy r-process ejecta (a.k.a. dynamical ejecta) and either a high- ($Y_e = 0.37$) or mid- ($Y_e = 0.27$) latitude wind composition. The mid-latitude composition contains a trace abundance of lanthanides, while the high-latitude model produces no lanthanides. The morphology of these two components are set using the TS and TP profile shapes from a more extensive morphology study (Korobkin et al. 2020). These two morphologies assume a toroidal profile for dynamical ejecta and either a spherical or peanut-shaped profile for the wind. The light curves from these models use the `SuperNu` (Wollaeger & van Rossum 2014) code that has now been run in a wide range of supernova and kilonova studies (Wollaeger et al. 2018; Even et al.

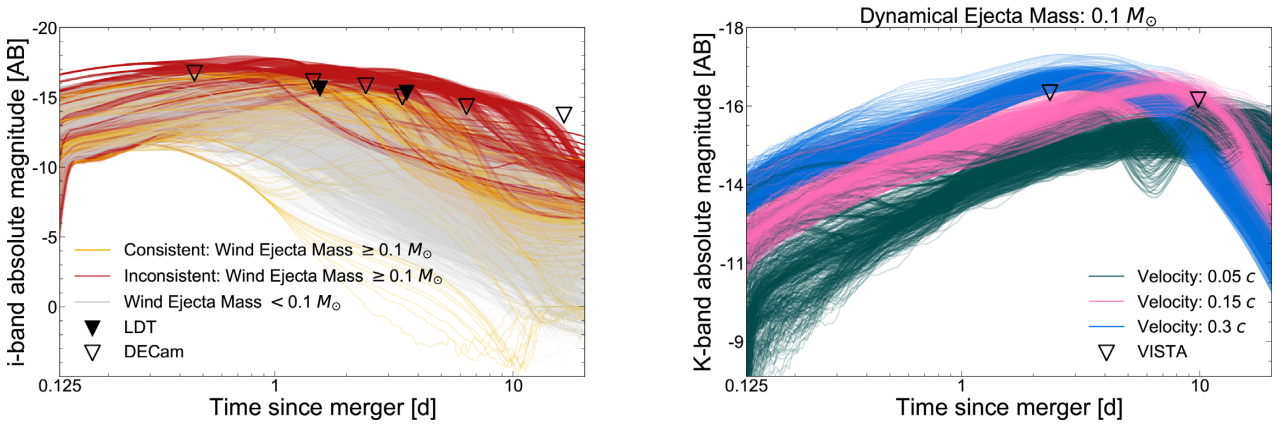

Figure 9. Kilonova light curves from LANL simulation suite. For clarity, only 11 of the 54 viewing angles are presented, spanning every fifth angular bin of equal solid angle ranging from viewing angles of 0° to 180°. Left-hand panel: *i*-band light curves for all kilonova parameters considered in the simulation space. Light curves are coloured by wind ejecta mass, with coloured (red or yellow) light curves containing a wind-mass of 0.1 $M_\odot$ and grey light curves corresponding to kilonova with smaller wind ejecta masses. Wide-field upper limit constraints (open triangles) divide the light curves into those inconsistent with observational constraints (red) and those that remain feasible (yellow). Galaxy-targeted LDT upper limits (solid triangles) are not used to constrain parameters. Right-hand panel: *K*-band light curves with dynamical ejecta masses of 0.1 $M_\odot$, with all other kilonova properties still allowed to vary. Light curves are differentiated by average dynamical ejecta velocity with the highest velocity in blue, intermediate velocity in pink, and lowest velocity in dark-green.

2019; Wollaeger et al. 2019; Korobkin et al. 2020). `SuperNu` is a multidimensional, multigroup Monte Carlo transport scheme, which produces light curves for a broad range of viewing angles. In addition, we employ the WinNet nucleosythesis network (Winteler et al. 2012) to simulate heating from radioactive decay of our prescribed abundances. The opacities use the latest LANL opacity data base: a full set of lanthanide opacities from Fontes et al. (2020) with uranium acting as a proxy for the full set of actinides. The grid of models includes two morphologies and two wind compositions in addition to a range of dynamical ejecta and wind masses (0.001, 0.003, 0.01, 0.03, 0.1 $M_\odot$). The grid also includes ejecta velocities of 0.05*c*, 0.15*c*, and 0.3*c*, corresponding to peak ejecta velocities of 0.1*c*, 0.3*c*, and 0.6*c*. The grid varies all six parameters independently, creating 900 different explosion models. Light curves depend on the viewing angle due to non-spherical morphologies; thus, we consider 54 different viewing angles for each model. The 54 polar viewing angles range from on-axis (0°) through edge-on (90°) and back to on-axis (180°), subtending an equal solid angle in each angular bin. Light curves are not binned in the azimuthal direction, due to the axisymmetric nature of the simulations. Including the angular dependence, we have 48 600 different sets of time-dependent kilonova spectra in our simulation data base to compare to the observational constraints.

4.3.2 Model comparison to data

This work expands upon past studies of GW190814 by both including the full set of observational limits and utilizing a broad grid of two-component models with realistic opacities. Our state-of-the-art grid produces a much more diverse set of light curves than past studies of these events. In this section, we assume negligible contamination from any GRB afterglows and that the possible kilonova dominates the observed *i*, *r*, *J*, and *K*-band emission. As discussed in the previous section, this assumption is well justified by the lack of any on-axis GRB as well as the expected faintness of an off-axis afterglow component.

Wide-field upper limits place the most compelling constraints on the data, and will be the focus of our kilonova parameter constraints. We direct our analysis to DECam upper limits in the *i*-band, VST upper limits in the *r*-band, and the VISTA upper limits in *K*-band. All upper limits are scaled to absolute magnitudes assuming a median luminosity distance of 267 Mpc.

Fig. 9 shows a subset of simulated *i* (left-hand panel) and *K*-band (right-hand panel) light curves (11 of the 54 viewing angles) compared to observational constraints. These light curves follow many of the same trends expected in transients. For example, models with faster ejecta velocities expand more quickly, causing earlier rise and fall times as well as brighter peak emission. The early-time *i*-band emission is dominated by the wind ejecta ('blue' component) and the late time *K*-band emission is dominated by the dynamical ejecta ('red' component). In an ideal scenario, observations would reveal a simple correspondence between *i*-band luminosity and the wind ejecta mass/velocity and, similarly, a relation between *K*-band luminosity and dynamical ejecta mass/velocity. However, additional properties affect the emission and further obscure this relationship. These properties include distribution of ejecta (e.g. morphology), lanthanide curtaining where the dynamical ejecta obscures the wind material and alters the early-time emission, and variations in the abundances. In general, models with more ejecta mass are brighter and are thus ruled out by the upper limit constraints.

The *i*-band light curves (Fig. 9, left-hand panel) are dominated by the wind ejecta. The colour-coding is based on the wind ejecta mass: grey models correspond to simulations with ejecta masses below 0.1 $M_\odot$, coloured models to simulations with ejecta masses above 0.1 $M_\odot$. The high-mass ejecta models are further delineated by whether they are ruled out by the observed upper limits: red models have luminosities that exceed at least one upper limit (ruled out by the data), yellow models lie below all the wide-field data (consistent with the data).

The dynamical ejecta plays a more important role in shaping the *K*-band light curves (Fig. 9, right-hand panel). The fast-velocity (average velocity of 0.3*c*), 0.1 $M_\odot$ dynamical mass models are nearly all ruled out by the VISTA upper limit at ∼2.35 d. Roughly 35 per cent of all intermediate velocity (average velocity of 0.15*c*) models with 0.1 $M_\odot$ dynamical mass are inconsistent with the constraints at ∼9.85 d. Due to their later peak time, slightly more low-velocity models remain plausible.

As many factors contribute to the light-curve morphology, we cannot prescribe a one-to-one correspondence between upper limits

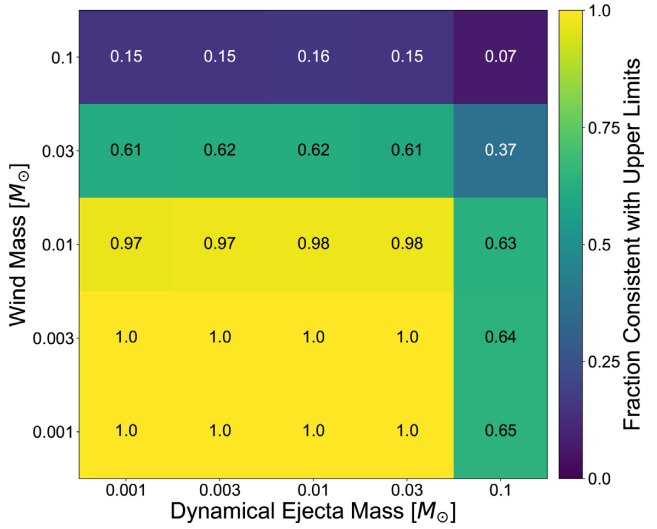

Figure 10. Fraction of simulated kilonovae consistent with wide-field upper limit constraints. We separate kilonova simulations by their input dynamical ejecta masses and wind masses. Each mass combination is represented by a colour and decimal fraction indicating the percentage of simulations for that given set of parameters that remain consistent with upper limits. We evaluate 1944 plausible kilonova simulations for each mass combination, with varying viewing angle, wind composition model, wind ejecta morphology, and velocities.

and a specific component of the ejecta. Fig. 10 shows the fraction of models consistent with the observed upper limits. Less than 15 per cent of our massive ($0.1\,M_\odot$) wind ejecta models are consistent with the data and only 7 per cent of these models with high dynamical ejecta masses ($0.1\,M_\odot$) lie below these limits. On the other extreme, all models with wind ejecta masses below $0.01\,M_\odot$ and dynamical ejecta masses below $0.1\,M_\odot$ are consistent with the data. Given the estimates of the BH mass (Abbott et al. 2020d), the constraints on the ejecta masses are consistent with the expectations from merger simulations.

Fig. 11 shows the fraction of consistent models studying different parameters. In these images, we reiterate many of the results seen in our light-curve models. Panel (a) demonstrates that the majority of fast (early-peaking), high-mass dynamical ejecta models are ruled out, as anticipated from the right-hand panel of Fig. 9. However, fast dynamical ejecta can obscure the signal from wind ejecta, and 34 per cent of the $0.1\,M_\odot$ slow-moving wind ejecta models are consistent with the observations versus only 6 per cent for the slow dynamical ejecta with comparable wind ejecta mass. Similarly, fast wind ejecta models both extend beyond the dynamical ejecta (this emission is not blocked) and peak brighter and earlier (ruled out by early observations). All fast-moving wind models with $0.1\,M_\odot$ wind mass ejecta are ruled out by the current constraints.

Of the 12 candidates with an unknown classification that have redshifts consistent with the GW distance scale (See Section 4.1), 10 have reported *i*-band detections and we compared them to our grid of simulated kilonova light curves. Two sources, AT2019tiw and AT2019tij, are inconsistent with all simulated kilonovae, remaining 2 magnitudes brighter than any plausible light curve. Some detections correspond to high wind ejecta masses ($\geq 0.1\,M_\odot$) and low wind velocities ($\leq 0.15c$). None of these candidates provide strong constraints on either dynamical ejecta mass or velocity.

We do not consider here the effects of the total extinction along the line of sight. However, we do not expect it to substantially change our conclusions since extinction is less important in the infrared band. Furthermore, short GRBs and GW170817 were found in sites of low extinction (e.g. Levan et al. 2017).

5 CONCLUSIONS

We have presented here our search for possible optical/nIR emission from GW190814. Our wide-field DDOTI observations covering 88 per cent of the probability area did not find a potential counterpart up to a limiting magnitude $w_{\rm max} \approx 19$ AB mag. Targeted observations of nearby galaxies were carried out using the Lowell Discovery Telescope, and did not identify any candidate counterpart down to $i = 22.9$ AB mag. Additionally, our RATIR and GTC observations focused on classification of candidates through multicolour photometry and spectroscopy, respectively. We could not find any association to a possible kilonova for all the candidates that were covered by these observations.

A total of 85 optical transients, with brightness ranging between 18 and 24 AB mag, were identified by other searches as possible counterparts of GW1901814. We find that about 75 per cent of these can be ruled out, while the remaining 21 objects are left unclassified. We find the follow-up observations to be very thorough within the first four days post-merger, with ∼67 per cent of the candidates announced in this period having a spectroscopic classification. A successful source identification was less likely at later times. These findings highlight that, even for well-localized events of high-interest such as GW190814, the identification efficiency of the follow-up campaign is lower than its detection efficiency. In addition to the sensitivity of the observing facilities, other factors, such as variable observing conditions, limited allocated time, or delays in the source classifications, further reduce the chances to find and identify the GW counterpart.

We used our observations in conjunction with the community-wide follow-up observations to place constraints on the GRB afterglow emission and the kilonova parameter space for this event. On-axis afterglows are strongly disfavoured, which is in line with the non-detection of gamma-ray emission. Off-axis afterglow light curves are instead too faint to be meaningfully constrained. In particular, for an energetic explosion similar to GW170817, any viewing angle above 10 deg would be consistent with the observations.

Based on our extensive kilonova simulations grid, we could constrain a wide range of ejecta masses and velocities. We find that models with high wind masses ($0.1\,M_\odot$) and high dynamical ejecta masses ($\gtrsim 0.1\,M_\odot$) are disfavoured by the optical upper limits. Additionally, nIR upper limits disfavour fast moving ($\geq 0.3c$) dynamical ejecta, assuming the dynamical ejecta mass to be $0.1\,M_\odot$.

Thanks to the large set of kilonova simulations, we find that a broader range of ejecta masses can be consistent with the data than past studies. For example we can not rule out all of our models with $0.1\,M_\odot$ ejecta (although we rule out most of these high-mass models). But the observations do rule out most of the wind ejecta (high electron fraction material from the disc) models above $0.1\,M_\odot$ and the fast-moving, high-mass dynamical ejecta (low electron fraction). These constraints are consistent with the latest models of ejecta masses from NSBH mergers (Fernández et al. 2020).

The recently published parameter values for this merger, a $23\,M_\odot$ BH merging with a $2.6\,M_\odot$ compact object, have interesting implications for the possible EM counterparts, supporting scenarios that encompass little or negligible ejecta. The high mass ratio suggests that there is a low chance of remnant matter outside the final object

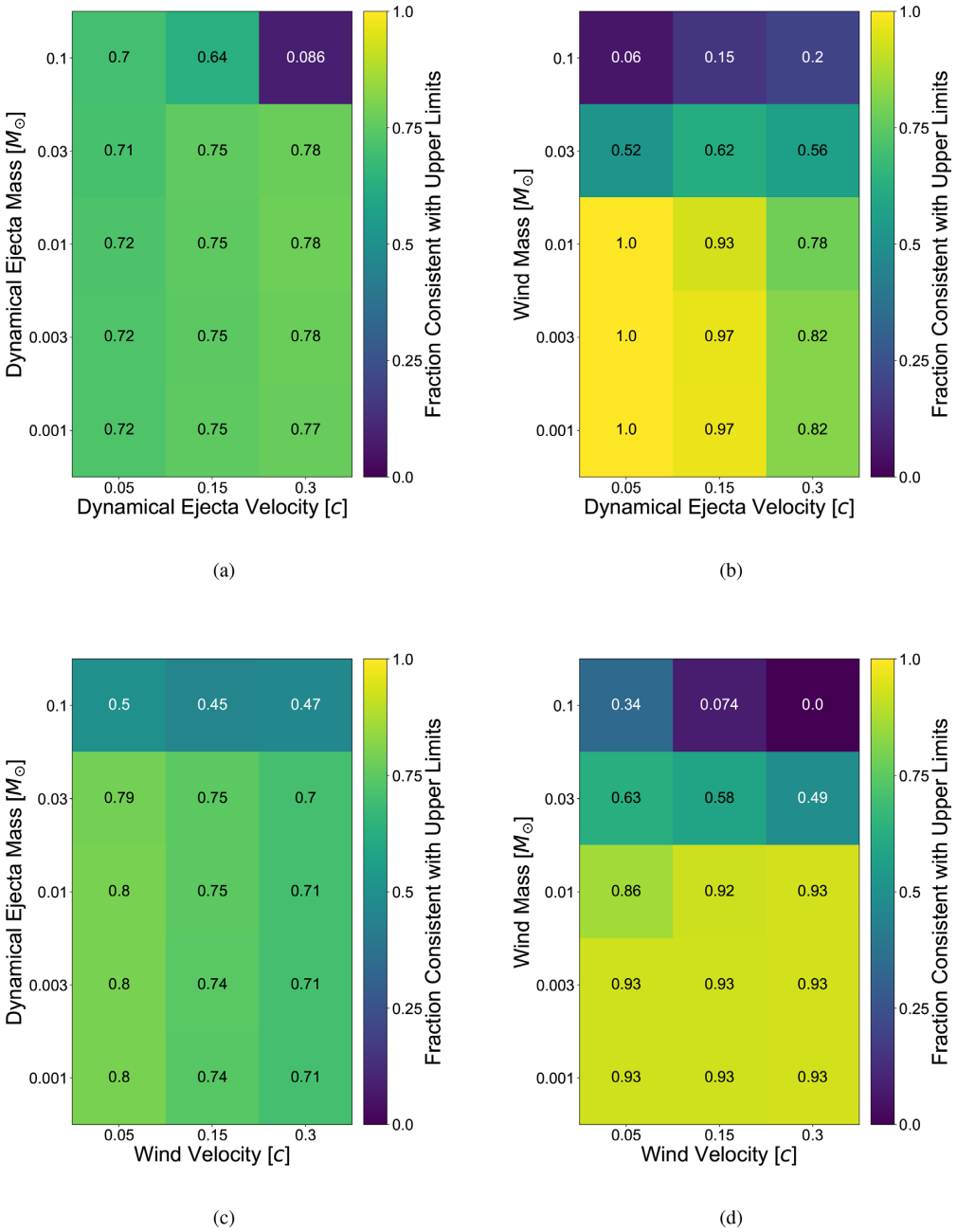

Figure 11. Fraction of simulated kilonovae consistent with wide-field upper limit constraints. Constrains are displayed jointly for each combination of mass and velocity parameters. Each parameter combination is represented by 3240 plausible kilonova simulations, with varying viewing angle, wind composition model, wind ejecta morphology, and masses and velocities not directly shown in each subfigure. The following parameter combinations are displayed: (a) dynamical eject mass and velocity, (b) wind mass and dynamical ejecta velocity, (c) dynamical ejecta mass and wind velocity, and (d) wind mass and velocity.

as the more massive BH will likely directly absorb the secondary component without its disruption. Furthermore, the nature of the secondary component is unclear from GW observations, and a low mass BH cannot be ruled out.

With the upcoming increase in sensitivity and addition of new detectors to the global GW network, we can expect future GW detections with smaller localization regions and at even farther distances (Abbott et al. 2018; Pankow et al. 2019). The case of GW190814 shows that, despite its good sky localization, small to medium aperture ground-based detectors are challenged at distance scales $\gtrsim$200 Mpc, and can only probe the brightest end of the luminosity distribution, corresponding to nearly-on axis GRB afterglows and high-mass kilonova ejecta. In the case of GW190814, the inclination angle of $\approx$45 deg and the high mass ratio of the binary components derived from the GW signal are not favourable to the detection of an EM counterpart, consistent with the lack of any suitable candidate from an extensive follow-up campaign. Information on the merging binary properties, such as its inclination and mass ratio, would therefore be a critical input for the observing community in order to optimize the use of observational resources as well as the subsequent effort of data analysis and source classification.

ACKNOWLEDGEMENTS

ALT, RSR, and LP acknowledge support from the European Union's Horizon 2020 Programme under the AHEAD2020 project (grant agreement n. 871158) and by ASI (Italian Space Agency) through the Contract no. 2019-27-HH.0 and from MIUR (PRIN 2017 grant 20179ZF5KS). SD and ET acknowledge support for this work under NASA grant 80NSSC18K0429. JBG acknowledges the support of the Viera y Clavijo program funded by ACIISI and ULL. GB acknowledges financial support under the INTEGRAL ASI-INAF agreement 2019-35-HH.0.

We thank Charlie Hoy for his help in accessing and loading the finalized GW190814 skymap.

We thank the staff of the Observatorio Astronómico Nacional. Some of the data presented in this paper were acquired with the DDOTI instrument of the Observatorio Astronómico Nacional on the Sierra de San Pedro Mártir. DDOTI is funded by CONACyT (LN 260369, LN 271117, and 277901), NASA Goddard space Flight center, the University of Maryland (NNX17AK54G), and the Universidad Nacional Autónoma de México (CIC and DGAPA/PAPIIT IT102715, IG100414, AG100317, and IN109418) and is operated and maintained by the Observatorio Astronómico Nacional and the Instituto de Astronomía of the Universidad Nacional Autónoma de México. We acknowledge the contribution of Neil Gehrels to the development of DDOTI.

Some of the data used in this paper were acquired with the RATIR instrument, funded by the University of California and NASA Goddard Space Flight Center, and the 1.5-m Harold L. Johnson telescope at the Observatorio Astronómico Nacional on the Sierra de San Pedro Mártir, operated and maintained by the Observatorio Astronómico Nacional and the Instituto de Astronomía of the Universidad Nacional Autónoma de México. We acknowledge the contribution of Leonid Georgiev and Neil Gehrels to the development of RATIR.

The spectroscopic data presented in this work were reduced using standard routines of PyRAF. PyRAF is a product of the Space Telescope Science Institute, which is operated by AURA for NASA. This research made use of `ccdproc`, an Astropy package for image reduction (Craig et al. 2017). This work made use of the data products generated by the NYU SN group, and released under DOI:10.5281/zenodo.58766, available at https://github.com/nyusngroup/SESNtemple/.

DATA AVAILABILITY

The data underlying this article will be shared on reasonable request to the corresponding author.

REFERENCES

Aasi J. et al., 2015, Class. Quantum Gravity, 32, 115012
Abbott B. P. et al., 2016, Phys. Rev. Lett., 116, 061102
Abbott B. P. et al., 2017a, Phys. Rev. Lett., 119, 161101
Abbott B. P. et al., 2017b, ApJ, 848, L12
Abbott B. P. et al., 2018, Living Rev. Relat., 21, 3
Abbott B. P. et al., 2019, Phys. Rev. X, 9, 031040
Abbott R. et al., 2020a, Phys. Rev. D, 102, 043015
Abbott R. et al., 2020b, Phys. Rev. Lett., 125, 101102
Abbott B. P. et al., 2020c, ApJ, 892, L3
Abbott R. et al., 2020d, ApJ, 896, L44
Acernese F. et al., 2015, Class. Quantum Gravity, 32, 024001
Ackley K. et al., 2020, preprint (arXiv:2002.01950)
Andreoni I. et al., 2019, GCN Circ., 25362, 1
Andreoni I. et al., 2020, ApJ, 890, 131
Baldwin J. A., Phillips M. M., Terlevich R., 1981, PASP, 93, 5
Barbieri C., Salafia O. S., Colpi M., Ghirlanda G., Perego A., 2020a, preprint (arXiv:2002.09395)
Barbieri C., Salafia O. S., Perego A., Colpi M., Ghirlanda G., 2020b, Eur. Phys. J. A, 56, 8
Barbon R., Benetti S., Cappellaro E., Rosino L., Turatto M., 1990, A&A, 237, 79
Barnes J., Kasen D., 2013, ApJ, 775, 18
Bertin E., Arnouts S., 1996, A&AS, 117, 393
Bilicki M., Jarrett T. H., Peacock J. A., Cluver M. E., Steward L., 2013, ApJS, 210, 9
Blondin S., Tonry J. L., 2007, ApJ, 666, 1024
Bruun S. H. et al., 2019, GCN Circ., 25384, 1
Butler N. et al., 2012, in McLean I. S., Ramsay S. K., Takami H., eds, Proc. SPIE Conf. Ser. Vol. 8446, International Society for Optics and Photonics. SPIE, Bellingham, p. 336
Calzetti D., Kinney A. L., Storchi-Bergmann T., 1994, ApJ, 429, 582
Calzetti D., Armus L., Bohlin R. C., Kinney A. L., Koornneef J., Storchi-Bergmann T., 2000, ApJ, 533, 682
Cepa J. et al., 2000, in Iye M., Moorwood A. F. M., eds, Proc. SPIE Conf. Ser. Vol. 4008, International Society for Optics and Photonics. SPIE, Bellingham, p. 623
Chambers K. C. et al., 2016, preprint (arXiv:1612.05560)
Cowperthwaite P. S., Berger E., 2015, ApJ, 814, 25
Craig M. et al. , 2017, astropy/ccdproc: v1.3.0.post1. Available at: https://doi.org/10.5281/zenodo.1069648
Dálya G. et al., 2018, MNRAS, 479, 2374
de Jaeger T. et al., 2018, MNRAS, 478, 3776
Dichiara S. et al., 2019, GCN Circ., 25352, 1
Dichiara S., Troja E., O'Connor B., Marshall F. E., Beniamini P., Cannizzo J. K., Lien A. Y., Sakamoto T., 2020, MNRAS, 492, 5011
Dimitriadis G. et al., 2019, GCN Circ., 25395, 1
Dobie D. et al., 2019, ApJ, 887, L13
Doctor Z. et al., 2017, ApJ, 837, 57
Drout M. R. et al., 2017, Science, 358, 1570
Etienne Z. B., Liu Y. T., Shapiro S. L., Baumgarte T. W., 2009, Phys. Rev. D, 79, 044024
Evans P. A. et al., 2017, Science, 358, 1565
Even W. et al., 2020, ApJ, 899, 24
Fernández R., Foucart F., Lippuner J., 2020, MNRAS, 497, 3221
Fontes C. J., Fryer C. L., Hungerford A. L., Wollaeger R. T., Korobkin O., 2020, MNRAS, 493, 4143
Foucart F., Hinderer T., Nissanke S., 2018, Phys. Rev. D, 98, 081501
Freedman W. L. et al., 2020, ApJ, 891, 57
Gal-Yam A., 2017, in Alsabti AW., Murdin P., eds, Handbook of Supernovae. Springer, Cham, p. 195
Gehrels N., Cannizzo J. K., Kanner J., Kasliwal M. M., Nissanke S., Singer L. P., 2016, ApJ, 820, 136
Goldstein D. A. et al., 2019a, GCN Circ., 25391, 1
Goldstein D. et al., 2019b, GCN Circ., 25393, 1
Golkhou V. Z., Butler N. R., Strausbaugh R., Troja E., Kutyrev A., Lee W. H., Román-Zúñiga C. G., Watson A. M., 2018, ApJ, 857, 81
Gomez S. et al., 2019, ApJ, 884, L55
Graham M. J. et al., 2020, Phys. Rev. Lett., 124, 251102
Granot J., Panaitescu A., Kumar P., Woosley S. E., 2002, ApJ, 570, L61
Hallinan G. et al., 2017, Science, 358, 1579
Henden A. A., Levine S., Terrell D., Welch D. L., Munari U., Kloppenborg B. K., 2018, in American Astronomical Society Meeting Abstracts, Vol. 232, p. 223.06
Herner K. et al., 2019, GCN Circ., 25373, 1
Jin Z.-P. et al., 2018, ApJ, 857, 128
Kasen D., Badnell N. R., Barnes J., 2013, ApJ, 774, 25
Kasen D., Fernández R., Metzger B. D., 2015, MNRAS, 450, 1777
Kasen D., Metzger B., Barnes J., Quataert E., Ramirez-Ruiz E., 2017, Nature, 551, 80
Kawaguchi K., Kyutoku K., Nakano H., Okawa H., Shibata M., Taniguchi K., 2015, Phys. Rev. D, 92, 024014

Kawaguchi K., Shibata M., Tanaka M., 2020, ApJ, 893, 153
Kewley L. J., Groves B., Kauffmann G., Heckman T., 2006, MNRAS, 372, 961
Korobkin O. et al., 2020, preprint (arXiv:2004.00102)
Krüger C. J., Foucart F., 2020, Phys. Rev. D, 101, 103002
Lee W. H., Ramirez-Ruiz E., 2007, New J. Phys., 9, 17
Lee W. H., Ramirez-Ruiz E., van de Ven G., 2010, ApJ, 720, 953
Levan A. J. et al., 2017, ApJ, 848, L28
Li L.-X., Paczyński B., 1998, ApJ, 507, L59
Liu Y., Modjaz M., 2014, preprint (arXiv:1405.1437)
Liu Y.-Q., Modjaz M., Bianco F. B., Graur O., 2016, ApJ, 827, 90
Lopez-Cruz O. et al., 2019, GCN Circ., 25571, 1
LVC, 2019a, GCN Circ., 25324, 1
LVC, 2019b, GCN Circ., 25333, 1
Metzger B. D., 2019, Living Rev. Relat., 23, 1
Miller J. M. et al., 2019, Phys. Rev. D, 100, 023008
Modjaz M., Liu Y. Q., Bianco F. B., Graur O., 2016, ApJ, 832, 108
Monet D. G. et al., 2003, AJ, 125, 984
Muendlein R., Li W., Yamaoka H., Itagaki K., 2005, Int. Astron. Union Circ., 8553, 1
Nissanke S., Kasliwal M., Georgieva A., 2013, ApJ, 767, 124
Nordin J., Brinnel V., Giomi M., Santen J. V., Gal-Yam A., Yaron O., Schulze S., 2019, Transient Name Server Discovery Report, 2019-1370, 1
O'Connor B., Beniamini P., Kouveliotou C., 2020, MNRAS, 495, 4782
Osterbrock D. E., 1989, Astrophysics of Gaseous Nebulae and Active Galactic Nuclei. University Science Books, Mill Valley
Palmer D. M. et al., 2019, GCN Circ., 25341, 1
Pankow C., Rizzo M., Rao K., Berry C. P. L., Kalogera V., 2019, preprint (arXiv:1909.12961)
Pannarale F., Tonita A., Rezzolla L., 2011, ApJ, 727, 95
Pian E. et al., 2017, Nature, 551, 67
Piranomonte S. et al., 2008, A&A, 491, 183
Piro L. et al., 2019, MNRAS, 483, 1912
Planck Collaboration et al., 2020, A&A, 641, A6
Poznanski D., Ganeshalingam M., Silverman J. M., Filippenko A. V., 2011, MNRAS, 415, L81
Poznanski D., Prochaska J. X., Bloom J. S., 2012, MNRAS, 426, 1465
Rosswog S., Feindt U., Korobkin O., Wu M.-R., Sollerman J., Goobar A., Martinez-Pinedo G., 2017, Class. Quantum Gravity, 34, 104001
Ruffert M., Janka H. T., 2010, A&A, 514, A66
Ryan G., van Eerten H., Piro L., Troja E., 2020, ApJ, 896, 166
Salmon L., Hanlon L., Jeffrey R. M., Martin-Carrillo A., 2020, A&A, 634, A32
Schechter P., 1976, ApJ, 203, 297
Schlafly E. F., Finkbeiner D. P., 2011, ApJ, 737, 103
Sekiguchi Y., Kiuchi K., Kyutoku K., Shibata M., Taniguchi K., 2016, Phys. Rev. D, 93, 124046
Shibata M., Taniguchi K., 2011, Living Rev. Relat., 14, 6
Shibata M., Uryu K., 2007, Class. Quantum Gravity, 24, S125
Shibata M., Fujibayashi S., Hotokezaka K., Kiuchi K., Kyutoku K., Sekiguchi Y., Tanaka M., 2017, Phys. Rev. D, 96, 123012
Singer L. P., Price L. R., 2016, Phys. Rev. D, 93, 024013
Singer L. P. et al., 2016, ApJ, 829, L15
Smartt S. J. et al., 2017, Nature, 551, 75
Tanaka M., Hotokezaka K., Kyutoku K., Wanajo S., Kiuchi K., Sekiguchi Y., Shibata M., 2014, ApJ, 780, 31
Tanaka M. et al., 2017, PASJ, 69, 102
Tody D., 1986, in Crawford D. L., ed., Proc. SPIE Conf. Ser. Vol. 627, The Iraf Data Reduction And Analysis System. SPIE, Bellingham, p. 733
Troja E. et al., 2016, ApJ, 827, 102
Troja E. et al., 2017, Nature, 551, 71
Troja E. et al., 2019, MNRAS, 489, 1919
Tucker D. et al., 2019, GCN Circ., 25379, 1
Turatto M., Benetti S., Cappellaro E., 2003, in Hillebrandt W., Leibundgut B., eds, Twilight to Highlight: The Physics of Supernovae. Springer, Berlin, p. 200
Typel S., Röpke G., Klähn T., Blaschke D., Wolter H. H., 2010, Phys. Rev. C, 81, 015803
Veitch J. et al., 2015, Phys. Rev. D, 91, 042003
Vieira N. et al., 2020, ApJ, 895, 96
Watson A. M. et al., 2012, in Stepp L. M., Gilmozzi R., Hall H. J., eds, Proc. SPIE Conf. Ser. Vol. 8444, International Society for Optics and Photonics. SPIE, Bellingham, p. 1787
Watson A. M. et al., 2016, in Peck A. B., Seaman R. L., Benn C. R., eds, Proc. SPIE Conf. Ser. Vol. 9910, International Society for Optics and Photonics. SPIE, Bellingham, p. 136
Watson A. M. et al., 2020, MNRAS, 492, 5916
Winteler C., Käppeli R., Perego A., Arcones A., Vasset N., Nishimura N., Liebendörfer M., Thielemann F. K., 2012, ApJ, 750, L22
Wollaeger R. T., van Rossum D. R., 2014, ApJS, 214, 28
Wollaeger R. T. et al., 2018, MNRAS, 478, 3298
Wollaeger R. T. et al., 2019, ApJ, 880, 22
Zwitter T., Munari U., Moretti S., 2004, Int. Astron. Union Circ., 8413, 1

[1]*INAF-Istituto di Astrofisica e Planetologia Spaziali, via Fosso del Cavaliere, 100, I-00133 Rome RM, Italy*
[2]*Dipartimento di Fisica, Università degli Studi di Roma 'Tor Vergata', Via della Ricerca Scientifica 1, I-00133 Roma RM, Italy*
[3]*Department of Astronomy, University of Maryland, College Park, MD 20742-4111, USA*
[4]*Astrophysics Science Division, NASA Goddard Space Flight Center, 8800 Greenbelt Rd, Greenbelt, MD 20771, USA*
[5]*Center for Theoretical Astrophysics, Los Alamos National Laboratory, Los Alamos, NM 87545, USA*
[6]*Computational Physics Division, Los Alamos National Laboratory, Los Alamos, NM 87545, USA*
[7]*Center for Interdisciplinary Exploration and Research in Astrophysics (CIERA), Northwestern University, Evanston, IL 60201, USA*
[8]*Department of Physics and Astronomy, Northwestern University, Evanston, IL 60208, USA*
[9]*Joint Institute for Nuclear Astrophysics - Center for the Evolution of the Elements, East Lansing, MI 48824, USA*
[10]*Computer, Computational, and Statistical Sciences Division, Los Alamos National Laboratory, Los Alamos, NM 87545, USA*
[11]*Steward Observatory, The University of Arizona, Tucson, AZ 85721, USA*
[12]*Department of Physics and Astronomy, The University of New Mexico, Albuquerque, NM 87131, USA*
[13]*The George Washington University, Washington, DC 20052, USA*
[14]*School of Earth and Space Exploration, Arizona State University, Tempe, AZ 85287, USA*
[15]*Instituto de Astronomía, Universidad Nacional Autónoma de México, Apartado Postal 70-264, 04510 México, CDMX, Mexico*
[16]*INAF-Istituto di Astrofisica Spaziale e Fisica Cosmica, Via Ugo la Malfa, 153, I-90146 Palermo PA, Italy*
[17]*Universidad de La Laguna, Dpto. Astrofísica, E-38206 La Laguna, Tenerife, Spain*
[18]*Instituto de Astrofísica de Canarias, E-38200 La Laguna, Tenerife, Spain*
[19]*Instituto de Ciencias Nucleares, Universidad Nacional Autónoma de México, Apartado Postal 70-543, 04510 CDMX, México*
[20]*Joint Space-Science Institute, University of Maryland, College Park, MD 20742, USA*
[21]*Scuola Universitaria Superiore IUSS Pavia, Piazza della Vittoria 15, I-27100 Pavia, Italy*
[22]*INAF, Istituto di Astrofisica Spaziale e Fisica Cosmica Milano, via A.,Corti 12, I-20133 Milano, Italy*
[23]*CONACYT, Instituto de Astronomía, Universidad Nacional Autónoma de México, 22860 Ensenada, BC, Mexico*
[24]*INAF-Istituto di Radioastronomia, Via Gobetti 101, I-40129 Bologna, Italy*
[25]*Istituto Nazionale di Ricerca Metrologica (INRiM), Strada delle Cacce 91, I-10135 Torino, Italy*
[26]*INFN, Sezione di Pavia, via A. Bassi 6, I-27100 Pavia, Italy*

This paper has been typeset from a TEX/LATEX file prepared by the author.